A conformable ultrasound patch for cavitation enhanced transdermal cosmeceutical delivery

by

Aastha Shah

B.S, Birla Institute of Science and Technology (2017)

M.Eng, University of California at Berkeley (2018)

Submitted to the Program in Media Arts and Sciences, School of Architecture and Planning, in partial fulfillment of the requirements for the degree of
Masters of Science
at the

MASSACHUSETTS INSTITUTE OF TECHNOLOGY

June 2023

Author

……..…….....

Aastha Shah
Department of Media Arts and Sciences
May 19, 2023

Certified by

…….....

Canan Dagdeviren
Associate Professor of Media Arts and Sciences, Thesis Supervisor

Accepted by

…….....

Tod Machover
Muriel R. Cooper Professor of Music and Media
Academic Head, Program in Media Arts and Sciences

A conformable ultrasound patch for cavitation enhanced transdermal cosmeceutical delivery

by

Aastha Shah

Submitted to the Program in Media Arts and Sciences,
School of Architecture and Planning
on May 19th, 2023, in partial fulfillment of the
requirements for the degree of
Masters of Science

Abstract

Increased consumer interest in healthy-looking skin demands a safe and effective method to increase transdermal absorption of innovative therapeutic cosmeceuticals. However, permeation of small-molecule drugs is limited by the innate barrier function of the stratum corneum. Here, we report a conformable ultrasound patch (cUSP) that enhances transdermal transport of niacinamide by inducing intermediate-frequency sonophoresis in the fluid coupling medium between the patch and the skin. The cUSP consists of piezoelectric transducers embedded in a soft elastomer to create localized cavitation pockets (0.8 cm^2, 1 mm deep) over larger areas of conformal contact (20 cm^2). Multiphysics simulation models, acoustic spectrum analysis and high-speed videography are used to characterize transducer deflection, acoustic pressure fields and resulting cavitation bubble dynamics in the coupling medium. The final system demonstrates a 26.2-fold enhancement in niacinamide transport in a porcine model *in vitro* with a 10-minute ultrasound application, demonstrating suitability of the device for short-exposure, large-area application of sonophoresis for patients and consumers suffering from skin conditions and premature skin aging.

Thesis Supervisor: Canan Dagdeviren

Title: Associate Professor in Media Arts and Sciences

A conformable ultrasound patch for cavitation enhanced transdermal cosmeceutical delivery

by

Aastha Shah

The following people served as readers for this thesis:

Thesis Reader……..…….....

Canan Dagdeviren
Associate Professor of Media Arts and Sciences, Thesis Supervisor
Program in Media Arts and Sciences

Thesis Reader……..…….....

Giovanni Traverso
Karl Van Tassel (1925) Career Development Professor
Department of Mechanical Engineering

Thesis Reader……..…….....

Robert Langer
David H. Koch (1962) Institute Professor
Department of Chemical Engineering

Thesis Reader……..…….....

Hugh Herr
Professor of Media Arts and Sciences
Program in Media Arts and Sciences

Acknowledgements

My warmest thanks to my supervisor Dr. Canan Dagdeviren for her unfailing steely determination and strong leadership in bringing this project to completion, and for creating numerous opportunities for both scientific exploration and my personal learning and growth through the process. I would also like to thank my illustrious thesis committee - Prof. Traverso, Prof. Langer and Prof. Herr for their incredibly valuable and practical feedback.

My heartfelt gratitude to Chia-Chen Yu, my co-author on this paper, for her clear thought process, steady mindfulness and patience in charting out every step of the research. Of'course my warm thanks to Colin Marcus, wizard of PhysEECS, for his invaluable help with the cavitation experiments and experimental setups, and most importantly for revealing the thrill of uncompromising scientific inquiry down to the fundamental concepts of any problem.

I am extremely indebted to Dr. James Bales at the Edgerton center, and the brilliant personnel at the Koch Institute - Heather Amoroso, Jeff Wyckoff and Kathleen Cormier, whose support was largely instrumental to the success of our biological experiments. Finally, my thanks to my lovely family - Dr. Bharti Shah, Rajeev Shah and Jyotsna Shah for their support and love, and my Cantabridgian family Sven Wang and Daniel Gomez.

Happy days.

Table of Contents

Table of Figures

1. Introduction

1.1. Overview of transdermal drug delivery

Transdermal drug delivery offers an attractive alternative to conventional drug delivery methods of intravenous [1], [2] and oral administration [3], [4] due to non-invasiveness, topical administration method, steady dose rate, and convenience [5]–[9].

However, the penetration of drugs and cosmeceuticals through the skin is limited by the innate barrier function of the skin to protect the underlying tissue against external substances [10]–[12]. The skin is composed of several layers including the stratum corneum (SC), epidermis, dermis, and subcutaneous tissue. The SC is the outermost layer of the epidermis and is approximately 5-15 μm thick with a robust structure containing dead keratinocytes tightly packed in a continuous structure of lipid bilayers. To avoid repetition of concepts fundamental to sonophoresis, I refer the reader to Schoelhammers doctoral thesis [13], which provides a rigorous introduction on the benefit of transdermal drug delivery over alimentary and parenteral routes, as well as the biology of the barrier function of the skin.

In order to overcome the low permeability of the SC and improve the efficacy of transdermal drug delivery, a number of methods have been developed including mechanical, thermal or chemical enhancers [14]–[16], application of electric fields employing iontophoresis [17], electroporation [18] and sonophoresis [19]–[22] or combined strategies involving two or more of the above [23], [24]. Among the physical

enhancement methods, sonophoresis, which is the use of ultrasound for delivery of drugs to or through the skin, has shown promising results in improving local, regional, and systemic drug delivery [25], [26]. While results with electroporation and iontophoresis demonstrate comparable levels of sustained drug delivery, the advantage of sonophoresis lies in the wide range of control parameters it offers, for example, frequency, amplitude and power. These can be manipulated to achieve painless, minimally invasive transport of a large range of drug molecules, and to different penetration depths [27], [28].

1.2. Working physics of sonophoresis

The key phenomenon responsible for the enhancement is acoustic cavitation, which is defined as the nucleation, growth, oscillation, movement, and collapse of tiny bubbles when ultrasound is irradiated to a liquid [29]. This results in the structural disordering of the stratum corneum lipids and an increase in the transdermal pathways for the transport of small molecule drugs [20]. Acoustic cavitation can be induced using low frequency sonophoresis (LFS) (20 - 100 kHz), intermediate frequency sonophoresis (IFS) (100 kHz-1 MHz), or high frequency sonophoresis (HFS) (over 1 MHz) [30].

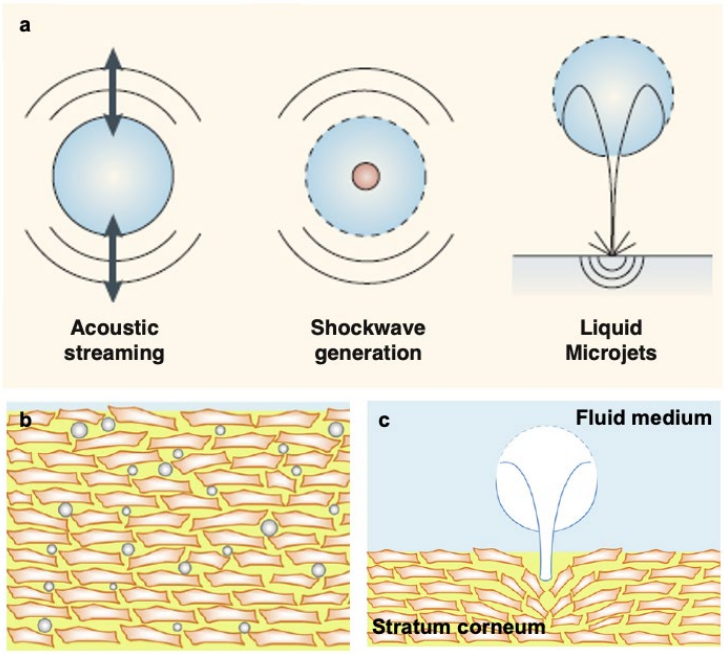

Figure 1 **a,** Three dominant bubble dynamics (left to right) - acoustic streaming with bubble movement through pressure gradients, shock wave generation during temporary bubble collapse, and permanent bubble collapse in a high-velocity microjet near a solid boundary. **b,** In-place oscillation of microbubbles within the stratum corneum with HFS. **c,** inertial collapse near solid boundary.

The resonant radii of the bubbles are inversely proportional to ultrasound frequency, and each frequency regime enhances skin permeability through different mechanisms (**Fig. 1 a-c**).

High-frequency sonophoresis: Traditionally, HFS has been the modality of choice and has been shown to improve penetration of small molecule drugs and their efficacy in vitro and in vivo [31], [32]. The small (< 20 μm) bubbles generated through HFS can be used to nucleate cavitation within the stratum corneum, where the bubble size is comparable to the intercellular distance of the lipid bilayers. However, at low acoustic pressures (~0.06 MPa), only stable cavitation events were observed with some repeated compression on cell boundaries, but the effect was insufficient to generate sonoporation within the skin [33]. However, stable cavitation does result in significant microstreaming or rapid circulatory movement of microbubbles, which increases the convective circulation if applied within a fluid. Strong inertial cavitation can certainly be attained with HFS at high acoustic pressures, but at a great cost on the energy demand of the process. The main benefits of HFS lie in three aspects - (1)

small bubble size which allows *in situ* membrane disruption without the need for a fluid coupling medium, (2) small transducer size (piezoelectric transducer thickness is inversely proportional to frequency), and (3) the low penetration depth of high-frequency ultrasound into tissue which localizes the effect to the topmost layers of the skin, giving HFS its long-standing history of safety and efficacy in trials *in vitro* and *in vivo* [30].

Low-frequency sonophoresis: However, it was later found that LFS, which generates larger bubbles (20–200 μm), could be more effective than HFS [34], [35] due to stronger transient phenomena such as shockwave generation, bubble collapse, and micro-jetting (**Fig. 1c**). Due to the large size of the bubbles, cavitation is unlikely to occur within the stratum corneum (thickness 15 μm), and the bubble effects in the fluid coupling medium at the surface of the skin become the main mechanism responsible for membrane permeabilization [21]. A study by Prausnitz [36] demonstrated through clear detection of the acoustic subharmonic spectrum that LFS (24 kHz) was capable of generating strong cavitation action even at moderate acoustic pressures (100 kPa). Further, the cavitation threshold for bubble nucleation (absolute negative pressure at which gas or water is vapourized within the fluid) is smaller at lower frequencies [37], [38].

Intermediate-frequency sonophoresis: Thus, the physics of acoustic cavitation seems to point in the direction of low-frequency ultrasound as the preferred modality for creating a significant mechanical disruption of the skin with moderate

demands on power. This is highly desirable from the point of view of designing lightweight, compact, wearable systems as is the goal of this report. In this report, we hypothesize that IFS can offer an interesting compromise between the convective effects (offered by HFS) and intensity of inertial cavitation (associated with LFS). As mentioned earlier, HFS treatments can be applied with the probe in direct contact with the skin, but the enhancement effects with lower frequencies cannot be obtained without a fluid coupling medium in between. It has also been demonstrated that membrane permeability is enhanced primarily by the cavitation action of bubbles directly above the skin, rather than in the bulk of the fluid [39]. This fact can be exploited from an ergonomic perspective to create small-volume wells of liquid couplants that provide a sufficiently large field for the onset of LFS between the transducer and the skin target. This phenomenon is leveraged in the design of the wearable patch discussed in this report, and elucidated further in **Section 1.4.**

1.3. Prior art

The table below lists previous works that use low frequency (20 kHz) and high frequency (1 MHz) sonophoresis to evaluate the permeation enhancement obtained with small as well as large molecule drugs *in vitro* and *in vivo*. Note that one of the studies employing HFS has the ultrasound probe positioned at a fixed distance from the target membrane, rather than in direct contact [40]. However, the bubble dynamics are not presented in the study, but we can assume that both convective as well as inertial effects may contribute to the permeation enhancement at the given power. Finally, we compare the device parameters and results from this work to the past

studies. The cUSP demonstrates superior performance in terms of compact form factor (soft, wearable interface), moderate power requirements (1 W/transducer), and minimal volume of fluid (0.4 ml/cm^2) required for obtaining comparable enhancement ratios (x26-fold) in the amount of drug delivered in comparison to previous works. Further, it clearly elucidates the bubble dynamics responsible for the enhancement effect observed, which distinguish it from other works that assess only the biological effect of the ultrasound modality in tissue without fully characterizing the cavitation physics. This report provides holistic characterization and transparency into the working physics of the sonophoresis modality used, which allows for better consequent manipulation of the system design parameters for achieving varied results for different applications.

Table 1 | Comparative analysis of parameters and results obtained with cUSP against other recent sonophoresis systems

Research work	**Frequency (kHz)**	**Power (W)**	**Duration (minutes)**	**Transducer type**	**Transd-ucer position-ing***	**Drug**	**Volume of fluid (ml/cm^2)**	**Enhancement**
				In vitro				
Mitragotri [40]	1000	2, 1	300	Commercial probe	~ 2.5cm	Multiple†	2.5	x2-15
Mitragotri [41]	20	7	10	Commercial probe	1 cm	Heparin	2	x21
Boucaud [42]	20	2.5	60	Commercial probe	1 cm	Fentanyl, Caffeine	1-1.3	x4-34
Manikkath [43]	20	7-8	30	Commercial probe	3-5 mm	Ketoprofen	2	x52
				In vivo				
Durmus [44]	1000	1.5	10	Commercial probe	Direct contact	Capsaicin	~3.14	Qualitative assessment only

Mitragotri [45]	20	7	2	Commercial probe	1 cm	Mannitol, Inulin	1.2	x33
Boucaud [46]	20	2.5	15	Commercial probe	1 cm	Insulin	0.95	2x decrease in blood glucose
Li [47]	1000	6	10	SEFM (stretchable electronic facemask)	Direct contact	Hyaluronic acid	N/A	Qualitative assessment only
This work (in vitro)								
Yu [48]	220	4-5	10	cUSP (bulk PZT-D in conformable substrate)	1 mm	Niacinamide	0.4	x26

* *Indicated transducer separation from target membrane*

† *Estradiol, testosterone, aldosterone, naphthol, lidocaine*

1.4. The cUSP interface

As per the discussion above, LFS and IFS are the modality of choice for achieving higher mechanical action with the cavitation regime. However, currently, delivering LFS/IFS to the target tissue involves completely submerging the target in the fluid or attaching flanged cylindrical fixtures to create ‘cavitation chambers’ on the skin surface [41], [42], which is not a feasible or scalable solution for non-medical applications. Further, manual positioning of the probe introduces high variability in treatment efficacy. This is not surprising given that acoustic cavitation is a highly sensitive stochastic phenomenon, where multiple system as well as environmental parameters such as transducer properties, spatial geometry [49] and choice of coupling medium [50], dissolved gas content [51], and heterogeneity and separation of target membrane profoundly impact each instance of cavitation. Thus, there is a need for a platform that can address the above issues and support the high-

enhancement inertial mechanisms offered by low frequency sonophoresis while maintaining conformal and flush contact with the skin.

In this report, we present a wearable solution to the above problem in the form of the cUSP. The conformable ultrasound patch (cUSP) consists of 4 piezoelectric elements (lead zirconate titanate (PZT)) embedded in a polydimethylsiloxane (PDMS) substrate. First, each PZT disc (PZT-D), with a diameter of 10 mm and thickness of 2 mm is separately coated with an ultra-thin PDMS layer using a precisely controlled dip-coating method. This creates a thin-film, waterproof encapsulation which provides minimal damping of the PZT-D motion in the fluid medium to allow maximum energy transfer. No backing or matching layers are added to the PZT-D as the objective of the design is to create large undamped peak pressures at a single driving frequency very close to the PZT-D surface, rather than maximize the energy transfer over a large frequency bandwidth and decrease the Q-factor, as is desirable for imaging transducers [52]. Four PZT-Ds are then arranged in a 2x2 array configuration with a center-to-center separation of 20 mm along with the serpentine metal (Cu) electrodes that establish their electrical connections. The system is placed in a custom 3D printed polylactic acid mold and fully encapsulated in a 2 mm thick PDMS layer. The PDMS encapsulation has square dimensions of 5 cm x 5 cm when it is initially demolded. For attachment onto the skin, the patch is trimmed to a circle of diameter of 5 cm. The CAD file is provided in the Supplementary Data. **Fig. 2 a, b** show the optical photograph of the cUSP attached on a glass cylinder and an exploded view of the multilayer construction of the patch, respectively.

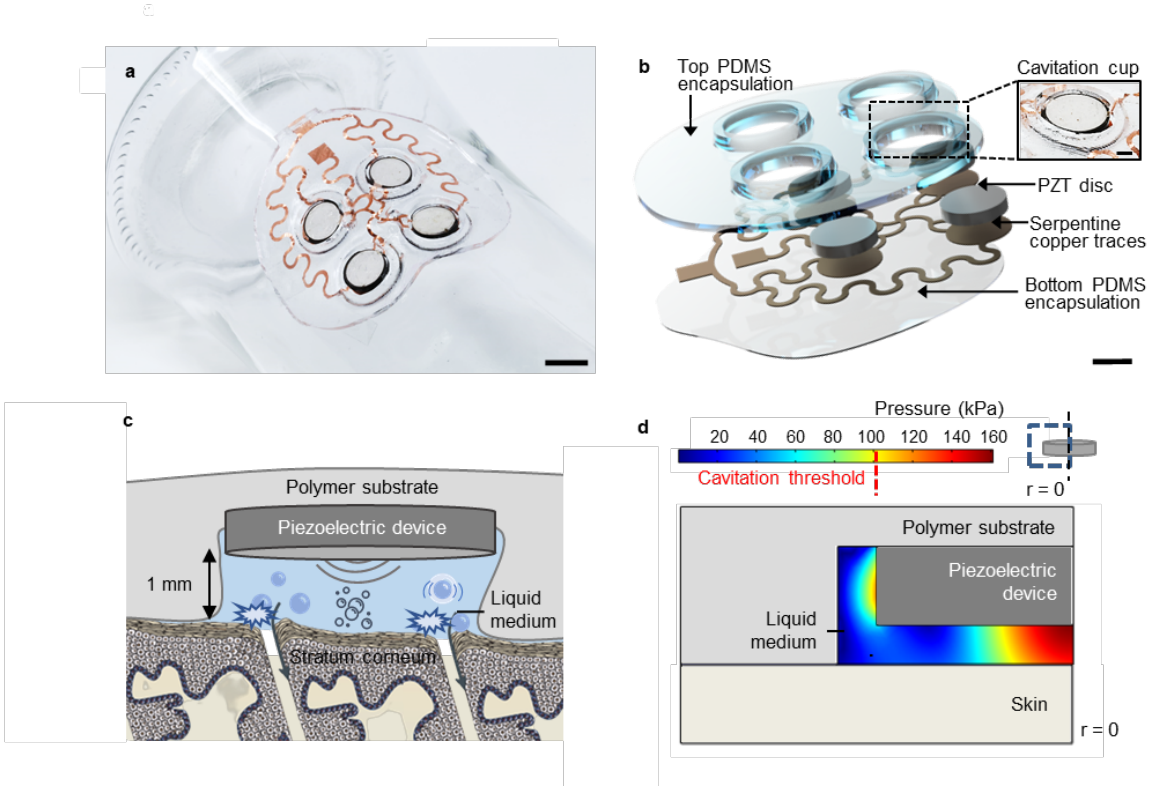

Figure 2 **a,** Photograph of the 2D-array of conformable ultrasound patch (cUSP) (diameter 5 cm, thickness 2 mm) attached to a curvilinear glass cylinder. Scale bar, 1 cm. **b,** Exploded view of the 2D-array of cUSP (5 cm x 5 cm x 2 mm) showing each constituent layer; Scale bar, 5mm (inset shows the fluid cavity formed between the PZT-D element and skin; Scale bar, 2 mm). **c,** Schematic illustration of the cUSP on skin, showing the cavitation mechanism within the cavity between the device and the skin, and resulting drug penetration through stratum corneum. Proportions of stratum corneum thickness to device size are distorted for the sake of clear illustration of the working mechanism. **d,** Acoustic pressure distribution in the device operating in radial mode at frequency of 212 kHz and applied voltage of 50 V, showing an undamped pressure zone (~100 kPa) within the medium in the cavity, which is enough to nucleate cavitation.

The distance of the ultrasound transducer from the target membrane shows an inverse relation with the count of bubbles [53]. Thus, the piezoelectric ultrasound transducer discs (PZT-D) are positioned in the substrate such that the disc surface is maintained at a small distance of 1 mm from the skin, while forming a cavity wherein the fluid medium can be contained (See inset in **Fig. 2b, Fig. 2c**). An annular gap of 1 mm width is maintained between the sides of the PZT-D and the surrounding PDMS substrate to allow undamped oscillation of the PZT-D in the radial direction, which is

the selected operating mode for the transducer as discussed in later sections. Ultrasound energy is applied to induce cavitation within this region as shown in the schematic illustration in **Fig. 2c.** An FEM simulation map of the acoustic pressure field with this geometry reveals that the pressure amplitude in the cavity is sufficient to nucleate cavitation [37], [54] and trigger violent bubble collapse [29] (**Fig. 1d**). It must be noted that while a theoretically predicted value of ~100 kPa is required to counter the atmospheric pressure (101.3 kPa) and trigger the degassing of dissolved air from an aqueous solution, in practice, the same effect may be achieved with lower pressures if impurities and gaseous nuclei are already present [38], [55]. This has been demonstrated in the subsequent sections.

2. cUSP (Conformable UltraSound Patch)

This section presents the full-spectrum characterization of the cUSP interface, starting with the electromechanical characterization of the PZT-Ds (**Section 2.1**), the acoustic pressure distribution (**Section 2.2**), cavitation detection (**Section 2.3**) and finally in vitro testing of the device to measure enhancement in drug transport (**Section 2.4**).

2.1. Electromechanical characterization of piezoelectric actuators

2.1.1. Simulated and experimental impedance profiles and modal shapes

Understanding the electrical impedance response of the PZT-D is fundamental to providing insight into the electrical behavior for a wide range of frequencies. The impedance magnitude depends on the structural and material properties and is a useful way to obtain vibration mode characterization since the electromechanical coupling factor and quality factor can be calculated from the impedance curve. The occurrence of natural frequencies of the piezoelectric transducer including both resonances (local minimums) and antiresonances (local maximums) can also be found via the impedance frequency spectrum.

The impedance from FEM simulations is calculated based on the ratio between voltage and current for the electrodes over the frequency range of interest. The total electric current flowing through the transducer is obtained by differentiating the charge density (Q) with respect to time (t) and integrating it over the electrode area. Electric charge is expressed in the exponential form of $Q = Q_o e^{i\omega t}$ which yields the current magnitude of $|I| = |\partial Q/\partial t| = \omega_o$, $Q = \int D_3 dA$, where D_3 is the electric displacement

in z direction and A is the surface area [56]. The impedance magnitude is then calculated by the general ohm law as $|Z| = |V| / |I|$. **Fig. 3a, b** shows the impedance spectra of the piezoelectric transducers with different dimensions obtained by the finite element method (FEM) analysis.

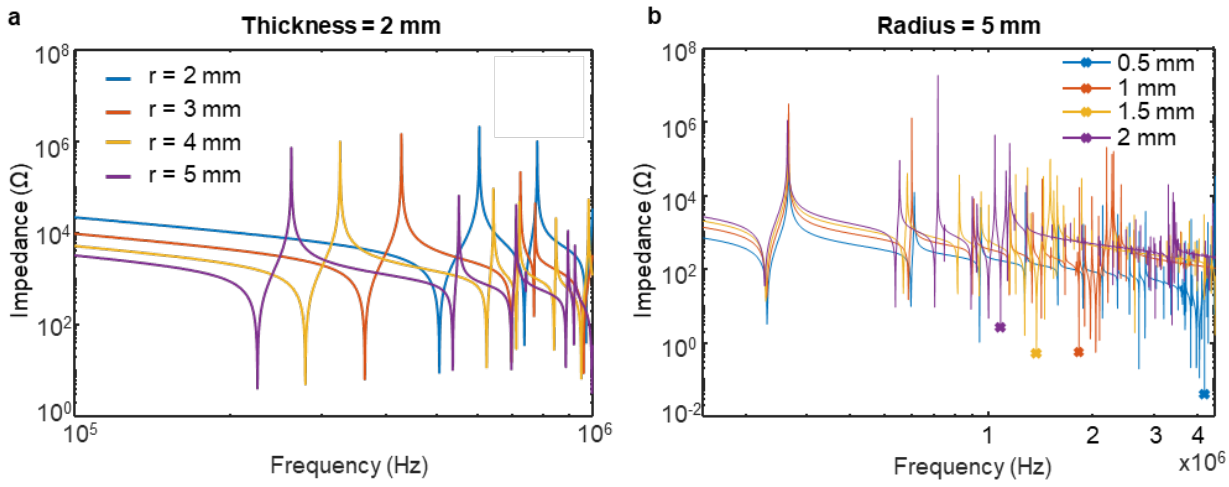

Figure 3 Impact of geometrical parameters on impedance of PZT-D. **a,** Impedance profile for various PZT-D radii for a fixed thickness of 2 mm. **b,** Impedance profile for various PZT-D thickness for a fixed radius of 5 mm.

The radius of the piezoelectric transducer is varied (2 mm, 3 mm, 4 mm, and 5 mm) while keeping the thickness constant at 2 mm to explore the effect of radial dimension on the impedance frequency spectrum. The lowest radial resonant frequency of 220 kHz is observed for the PZT-D with a radius of 5 mm. It is observed that increasing the radius of the piezo shifts the resonant frequency down from 550 kHz at 2 mm to 220 kHz at 5 mm as shown in **Fig. 3a**. However, the change in radius has a negligible impact on the resonant frequency of the thickness mode close to 1 MHz. Next, the radius is kept constant at 5 mm, and the thickness is varied between 0.5 - 2 mm. This significantly impacts the resonant frequency of the thickness mode (1.08 MHz at 2 mm to 4.18 MHz at 0.5 mm, marked with '-x' in **Fig. 3b**). This is in

accordance with the inverse relationship expected between the resonance frequency and thickness of the crystal. It is also to be noted that the resonance frequency at the radial mode (~220 kHz) remains relatively unchanged for thickness changes (5% variation between the minimum and maximum values, measured with respect to the minimum, 225 kHz). This demonstrates a strong decoupling between the thickness and radial modes of operation of the PZT-Ds, and can be strategically exploited in the design of the patch. For example, the radial mode can be selected as the operating mode of the device, and the thickness can be reduced significantly to achieve a more compact form factor without significantly shifting the resonant frequency and peak displacement attainable at that frequency (**Fig. 3b**). This is desirable from an operational point of view, as the cavitation threshold in a given medium depends strongly on the frequency of the ultrasound energy being applied.

For the PZT-D of interest, (r = 5 mm, t = 2 mm), we obtain 5 distinct modes in the range of 200 kHz to 1.1 MHz. An impedance analyzer (E4990A, Keysight Technologies) was used to experimentally determine the impedance characteristics of the device in air before fluid structure interactions. The measured impedance spectrum in the frequency domain is shown in **Fig. 4** along with that obtained by the FEM simulation. The lowest impedance values are obtained at 217 kHz and 1 MHz experimentally and at 225 kHz and 1.01 MHz from simulation. The slight shift (< 4%) in the resonant frequencies between simulation and experiment likely results from the damping effect of the copper electrodes on the piezoelectric transducer surface.

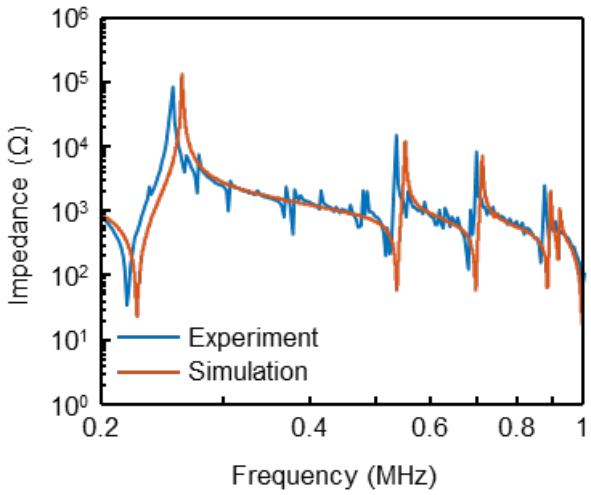

Figure 4 Experimental and simulated impedance profile for the PZT-D transducer used in cUSP

For the entire range of frequencies examined, the impedance values predicted by FEM simulations agree remarkably well with the experimental data as shown in **Fig. 4**. The resonant frequencies measured experimentally are slightly smaller than the FEM predicted values, which can be attributed to higher damping in the real-world scenario due to differences in air density and the copper-tape soldered electrical contacts made on the electrodes. It should be noted that there is an inherent device-to-device variation (< 1%) in the radial resonance frequency in the part as received from the supplier. For each time the disc is used, the exact resonance frequency is scoped in the neighborhood of 220 kHz to find the frequency corresponding to the lowest impedance value for the given disc, coating and environment, and this frequency is then selected for further operation of the device to obtain optimal energy transfer for that environment.

2.1.2. Simulated and experimental displacement profiles

Of the 5 modes discussed above, the PZT-D exhibits two dominant different types of deformations: radial and thickness. The radial mode involves expansions and contractions along the radius. The through thickness deformations are swellings in the thickness direction. We aim to numerically investigate the vibration characteristics and mode shape for both modes (radial and thickness modes). The free boundary conditions are applied to our FEM model. The relation between the voltage and displacement can be expressed as $-\rho\omega^2 u = \nabla.S$, $S = c:\epsilon - e^T E$ where ρ, ω, *u, S, c, e* and *E* are the density, frequency, displacement vector, strain, elasticity, coupling matrix, and electric field vector, respectively. The plots below show the variation in peak displacement obtained for various thicknesses of a PZT-D of radius 5 mm.

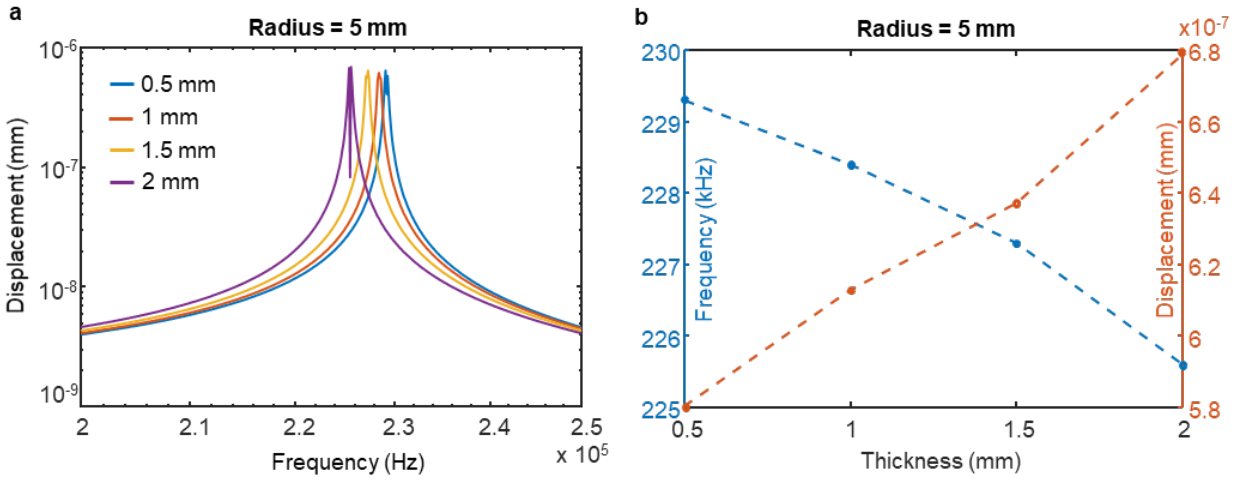

Figure 5 Displacement plots for PZT-Ds of varying thickness. **a,** Peak displacement of PZT-D element (at the center of the face) for different PZT-D thickness at a fixed radius of 5 mm**. b**, Shift in peak placement and resonance frequency for different PZT-D thickness for a fixed radius of 5 mm. The shift in resonance frequency is calculated for discrete values (solid dots), and the trend is extrapolated using the dashed lines.

The PZT-D of 5 mm radius and 2 mm thickness is used in the final design of the cUSP. Accordingly, the displacement profiles are characterized and compared for the two modes for this device going forward. The mode shapes and peak total displacements of the top surface of the PZT-D freely suspended in air are shown in **Fig. 6** for the 2 dominant resonance modes (f_r (220 kHz), and f_t (1,08 MHz)). The displacement is in the order of 1-20 nanometers for a 10 V_{pp} pure sinusoidal signal at the driving frequency. **Fig. 6** shows higher displacement peaks at f_r as compared to the value for a 2-mm thick PZT-D as shown in **Fig. 5a**. This can be attributed to the energy being focused in a narrow frequency band for multiple cycles for a continuous pure sine as compared to application for a single cycle at each frequency step in the case of a sweep.

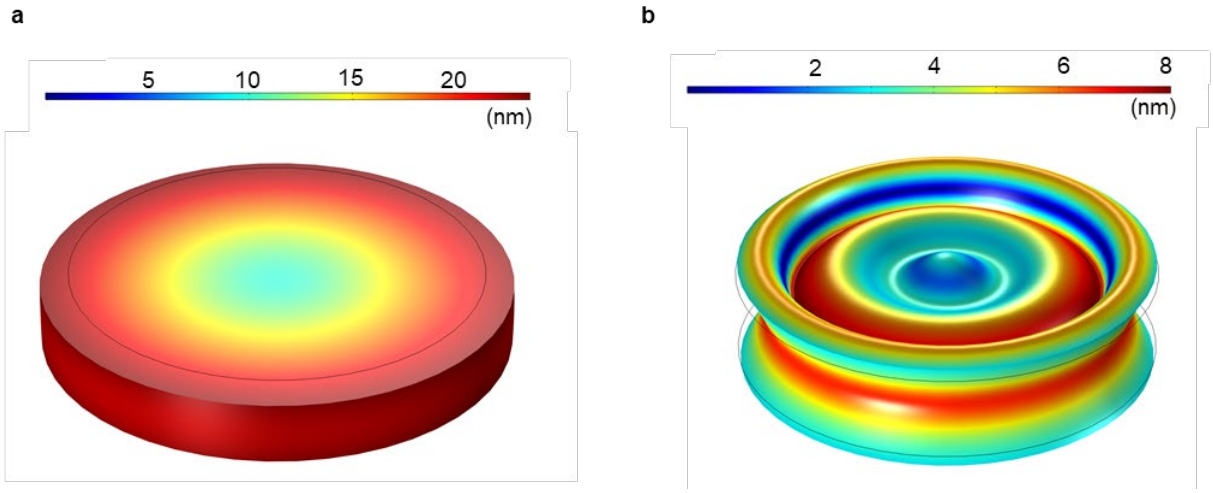

Figure 6 Mode shapes showing peak displacement in PZT-Ds (radius 5 mm, thickness 2 mm) **a,** radial mode and **b,** thickness mode

For the experimental measurements, the device is suspended in air and water under the three-dimensional laser doppler vibrometer (LDV, MSA-500, Polytec) measurement system to measure the deflection across the top surface of the PZT-D as shown in **Fig. 7**. The frequency is swept from 0.2-1 MHz and the shape modes are

reconstructed for the 2 resonant frequencies f_r ,f_t as given in **Fig. 7c,d.** The displacement plots from the simulated and experimental model in air are overlaid in **Fig. 7a** for a frequency sweep of 0.2-1 MHz.

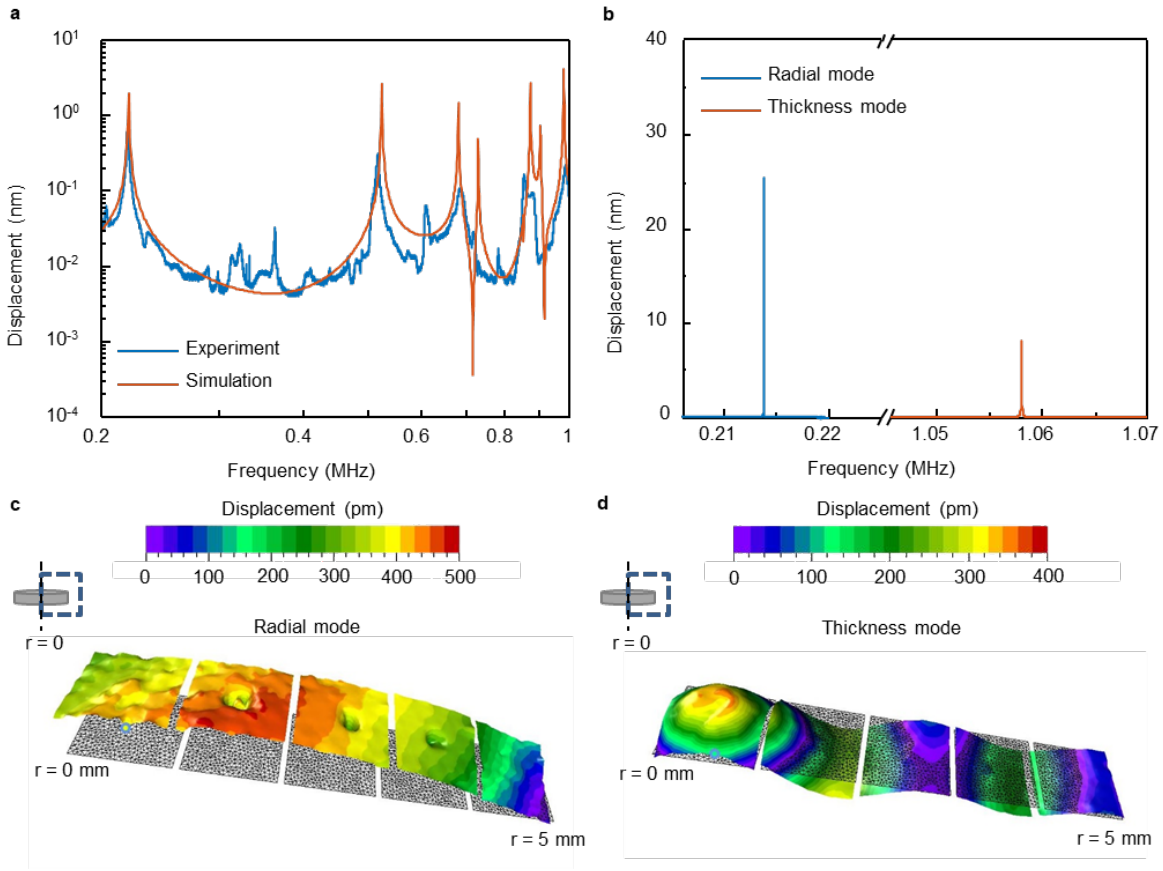

Figure 7 Experimentally measured displacement profiles for **a,** swept frequency (200 kHz-1 MHz) and **b,** continuous sine mode. **c, d,** Stitched image reconstruction on the laser vibrometer of the deflection of the top half-surface of the axisymmetric piezoelectric element (from r = 0 mm to r_{max} = 5 mm as shown in the thumbnail on the top left corner) to show the shape mode for f_r (radial mode) (d) and f_t (thickness mode). The colormap shows the z-displacement in picometers for a driving voltage of 10 V. Animations of the same are given in **Supplementary Video 1,2**.

The displacement under the effect of a continuous sinusoidal signal at the two resonance modes (f_r, f_t) is considered as the final system will be driven in a pulsed or continuous mode. **Fig. 7b** shows higher displacement peaks at the two resonant frequencies as compared to **Fig. 7a**. This again can be attributed to the energy being

focused in a narrow frequency band for multiple cycles for a continuous sine as compared to application for a single cycle at each frequency step in the case of a sweep. The shape mode for the maximum deformation of the top PZT-D surface presents the same number of nodes (3 anti-nodes at f_t, 1 anti-node at f_r (**Fig. 7c, d**)) as predicted by the FEM model (**Fig. 6a, b**). A similar measurement is performed with the PZT-D submerged in water, and a negligible shift in resonance frequency is observed (**Fig. 8**).

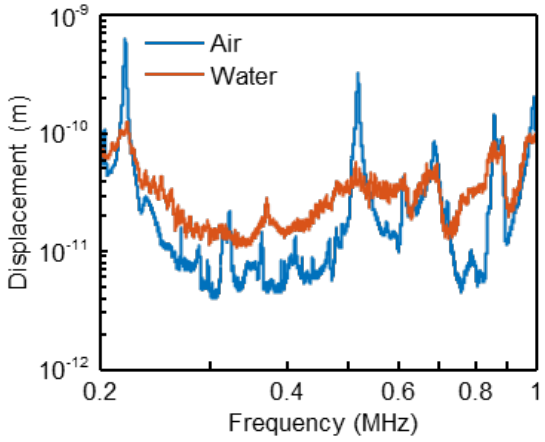

Figure 8 Displacement profile of PZT-D of interest (r = 5 mm, t = 2 mm) in air versus water for swept frequency (200 kHz - 1 MHz)

2.1.3. Impact of polymeric encapsulation

Addition of flexible substrates on piezoelectric transducers can not only provide mechanical stability but result in improved electromechanical response and flexibility. However, purely in terms of modal analysis, addition of a substrate to a piezoelectric transducer can significantly alter the vibrational behavior (natural frequency and modes) of the device due to a shift of the neutral axis. Therefore, the substrate material and geometry were selected such that the natural frequencies and vibrational modes

on the ultrasound modes are not altered significantly. PDMS serves as an excellent material for microfluidic devices. Properties such as resistance to biodegradation, chemical stability, biocompatibility and physiological indifference make it a good substrate material for ultrasound-based drug delivery devices. Moreover, for this particular application, the substrate acts as a good base for adhesive to maintain contact with the skin, and structurally patterned 1 mm-deep cavities around the PZT-D elements act as an active drug reservoir during sonophoresis. The PDMS substrate has a thickness of 1 mm which shifts the radial and thickness mode resonance frequencies to 225 kHz and 996 kHz respectively. The low thickness of the substrate is selected to minimize the shift of resonant frequencies compared to the initial radial (220 kHz) and thickness (1 MHz) modes of the substrate-free transducer. The addition of PDMS substrate ultimately results in an insignificant shift in the neutral axis while still providing mechanical stability and improved electromechanical response.

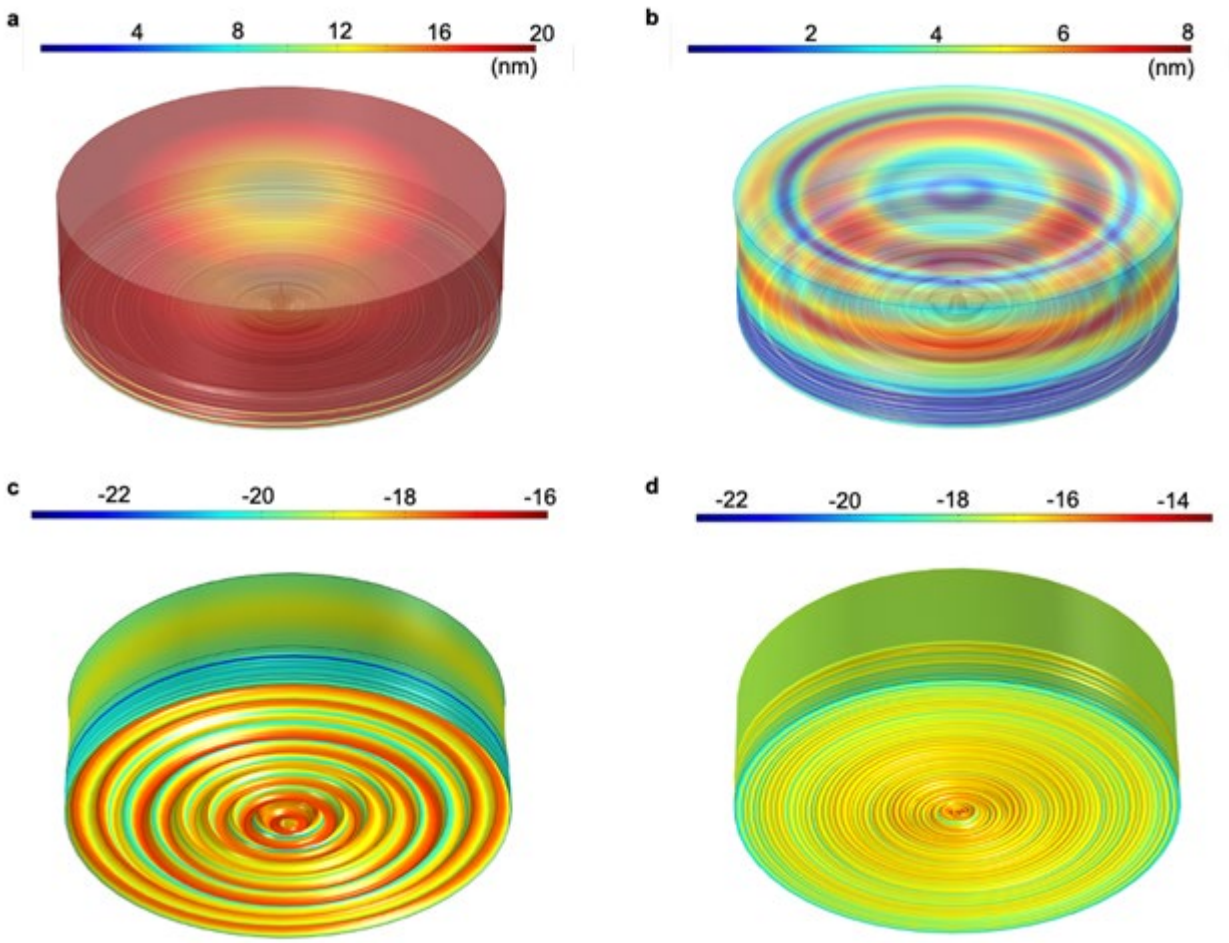

Figure 9 Impact of PDMS substrate on mode shape and displacement of the PZT-D. PZT-D with 1 mm-thick PDMS substrate at bottom, showing peak displacements (capped at 20 nm and 8 nm respectively) across the top surface of the PZT-D for **a,** radial (220 kHz) and **b,** thickness mode (1 MHz). The PZT-D is driven at 10 $V_{pp.}$ Log of displacement in PDMS substrate at the bottom of the PZT-D for **c,** radial and **d,** thickness mode.

Fig. 9 illustrates the impact of the PDMS substrate on the operational modes of the transducer. In the absence of the PDMS substrate, the PZT-D experiences low deformation due to the high stress and a bulk of the residual energy is dissipated. The addition of the PDMS layer allows for the dissipated energy to be translated to the substrate, resulting in significantly higher displacement in the PDMS layer. These values are 4 orders of magnitude larger than the PZT-D displacements, which follows from the ratio of the elastic moduli of the two materials (PDMS: 0.6 MPa, PZT: 60

GPa). The effect of the energy translation can be seen in the log scale **Fig. 9c,d,** where the bottom of the transducer is shown. However, there is no significant shift in the resonant frequencies of the PZT-Ds in the two cases (with and without PDMS backing substrate), and the displacements attained on the top surface of the PZT-D (the surface of interest coupled with the fluid medium and skin) remains undamped with the addition of PDMS (comparing with **Fig. 6a**), reaching a peak value at f_r of 20 nm in both cases. It is to be noted that in the final device, there is an additional thin encapsulation layer for each PZT-D element before it is assembled onto the cUSP substrate. (see **Appendix B1**). However, the thickness of this layer is in the range of 70-85 μm (**Appendix A1**) which is much smaller than the 1 mm-thick PDMS backing layer considered in **Fig. 9** and thus has a negligible impact on the PZT-D performance. Next, **Fig. 10** shows an overlay of the impedance spectrum of a single bare PZT-D, PZT-D with 1 mm-thick PDMS coating, and the cUSP (4 PZT-D elements in a 2D array, parallel configuration).

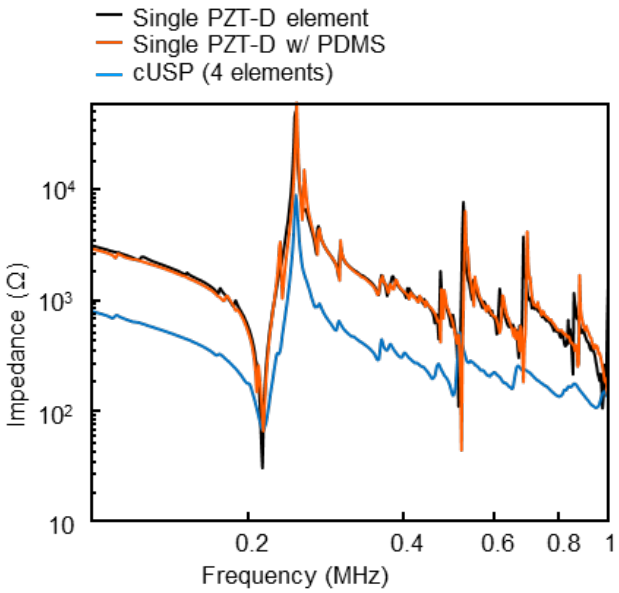

Figure 10 Impact of polymeric encapsulation on the impedance curve of single element PZT-D and cUSP array

An interesting observation can be made here. Since the 4 PZT-D elements are attached in parallel, we expect the impedance of the equivalent circuit to be $1/4^{th}$ that of a single element. Far away from the resonance peaks, it can be seen that the patch impedance is indeed shifted down to about 0.25x the single-element impedance values (for example, in the frequency range of 100-150 kHz in **Fig. 10**). However, near the resonant peaks, e.g. at 220 kHz, the patch impedance (67 Ω) is greater than that of a single element (30 Ω). This behavior is caused due to a change in the relative contributions of the electrical and mechanical components of the system in the different operating modes. Off-resonance, the curve is dominated by the high impedance values of the PZT-D discs. At resonance, the impedance of the PZT-D discs is dramatically reduced, and the impedance reading is dominated by the mechanical damping offered by the PDMS substrate, which is larger in the case of the cUSP as compared to PDMS-coated single element. It is critical to take into account this electro-mechanical coupling effect between the PZT-D and the substrate in order to correctly characterize the impedance value of the system and optimize the power transfer characteristics. The FEM results match well with the experiment and show that the numerical method can accurately characterize the vibrational behavior of the device, and can thus be extended to simulate fluid interactions. We investigate the pressure regime for both modes (f_r, f_t) in the following section to further consolidate the choice for the final operating mode of the device.

2.2. Acoustic pressure characterization

2.2.1. Experimental setup for acoustic pressure measurements using needle hydrophone

It is desirable to characterize the acoustic pressure fields close to the PZT-D to estimate the spatial likelihood of cavitation. However, measuring the pressure experimentally using a hydrophone (**Fig. 10**) is extremely sensitive to reflections in the measurement setup and coupling from the electromagnetic field close to the transducer.

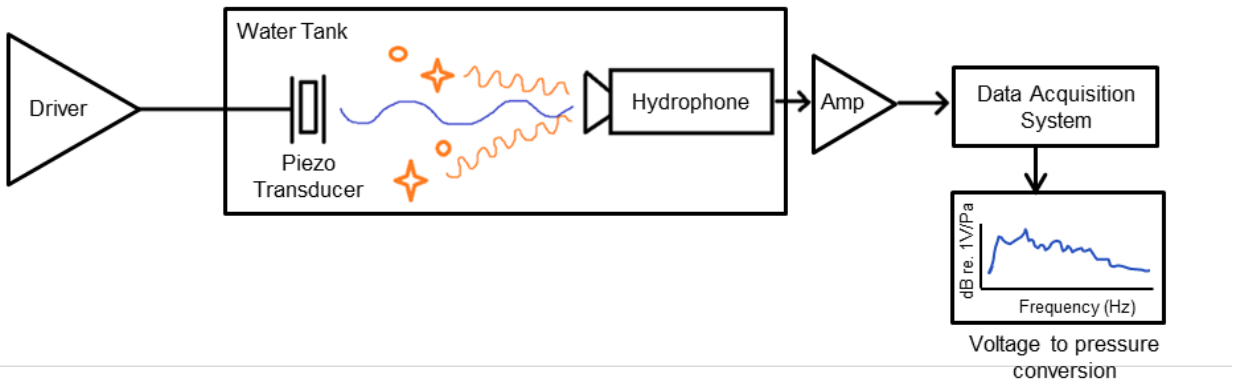

Figure 11 Schematic for experimental setup for measurement of acoustic pressure using a needle hydrophone

Here we aim to simulate various configurations of the measurement setup to determine the optimal boundary conditions in a water-tank to guarantee quality capture of hydrophone data. We then measure the pressure experimentally in this configuration, and compare the data with a simulated pressure-frequency sweep at fixed distance of 1, 2 and 3 cm from the transducer surface. This verified simulation model is then used to predict near-field pressure in the PDMS cavities for the final patch design, discussed subsequently in **Section 2.2.3**.

In order to solve the wave equation in the fluid media surrounding the piezo transducer, the physics interface of “Pressure Acoustics, Frequency Domain” interface module is added to the previous COMSOL Multiphysics FEA model developed for the numerical simulations. The physical field of acoustic pressure is explored in the frequency domain and contains the partial differential equations (PDEs) known as the Helmholtz equations described as the following wave equation:

$$\nabla \cdot \frac{-\nabla p(x,y)}{\rho} - \frac{\omega^2 p(x,y)}{c^2 \rho} = 0$$

where *ω, c,* and *ρ* represent the frequency of wave propagation, speed of the wave in the water, and density of water, respectively. and *p(x,y)* represents the scattered acoustic pressure field in terms of the Cartesian coordinate for the spatial domain (*x* and *y*). The model simply assumes that the acoustic source is made up of numerous point sources, with each point source contributing to the overall pressure field at that location, and it is used to produce the pressure field at frequencies matching the vibrational modes.

The lumped parameter electromechanical acoustic model can be expressed as [57]: $[K]\{u\} - \omega^2[M]\{u\} + \omega jZ(p, \omega)\{u\} = \{0\}$ where [K], [M] are matrices of stiffness and mass, {u} is the displacement, ω is the frequency, Z(p, ω) is the complex acoustic coupling dependent on the acoustic pressure p, and frequency.

Boundary conditions are critical constraints in COMSOL Multiphysics simulations. They are defined based on the pressure acoustics module considering

the sound hard boundary wall which assumes that the normal component of the acceleration, velocity, and the normal derivative of the pressure are zero at the boundary $\partial P_t/\partial n = 0$. The spherical wave radiation is a radiating field source located at $z_o = 0$. The water medium has a 10 cm x 10 cm surface area. We have tested three different boundary conditions which are shown in **Fig. 12**. The true absolute pressure measurements correspond to **Fig. 12a**, with plane-wave propagation conditions assigned to both the top (air-water surface) and side walls of the tank. This assumes that the water medium continues infinitely in both directions presenting no reflections, and the pressure field is representative of the true values. The amplitude of the pressure decreases gradually along z towards the air-water interface (**Fig. 12a**, right). Next, in **Fig. 12b**, we simulate the case of a water-air interface at top surface, and a reflective water-glass-air interface at the side walls. This creates a standing-wave pattern within the tank (**Fig. 12b**, left), and presents many time-varying artifacts in the pressure amplitude across the tank as seen in the plot given alongside which results in an over- or under-estimation of the true pressure at any given location. Next, we simulate a case with an open water tank (air-water interface at the top) and acoustic dampeners (AptFlex F28, Precision Acoustics) on the side walls to minimize reflections by assigning plane-wave propagation at the sides of the model tank (**Fig. 12c**). This case shows remarkable similarity with the ideal case in both the wave pattern and the rate of decrease of the pressure amplitude. This configuration is also feasible to set up in practicality, and is chosen to make the far-field pressure measurements shown in **Fig. 12d**.

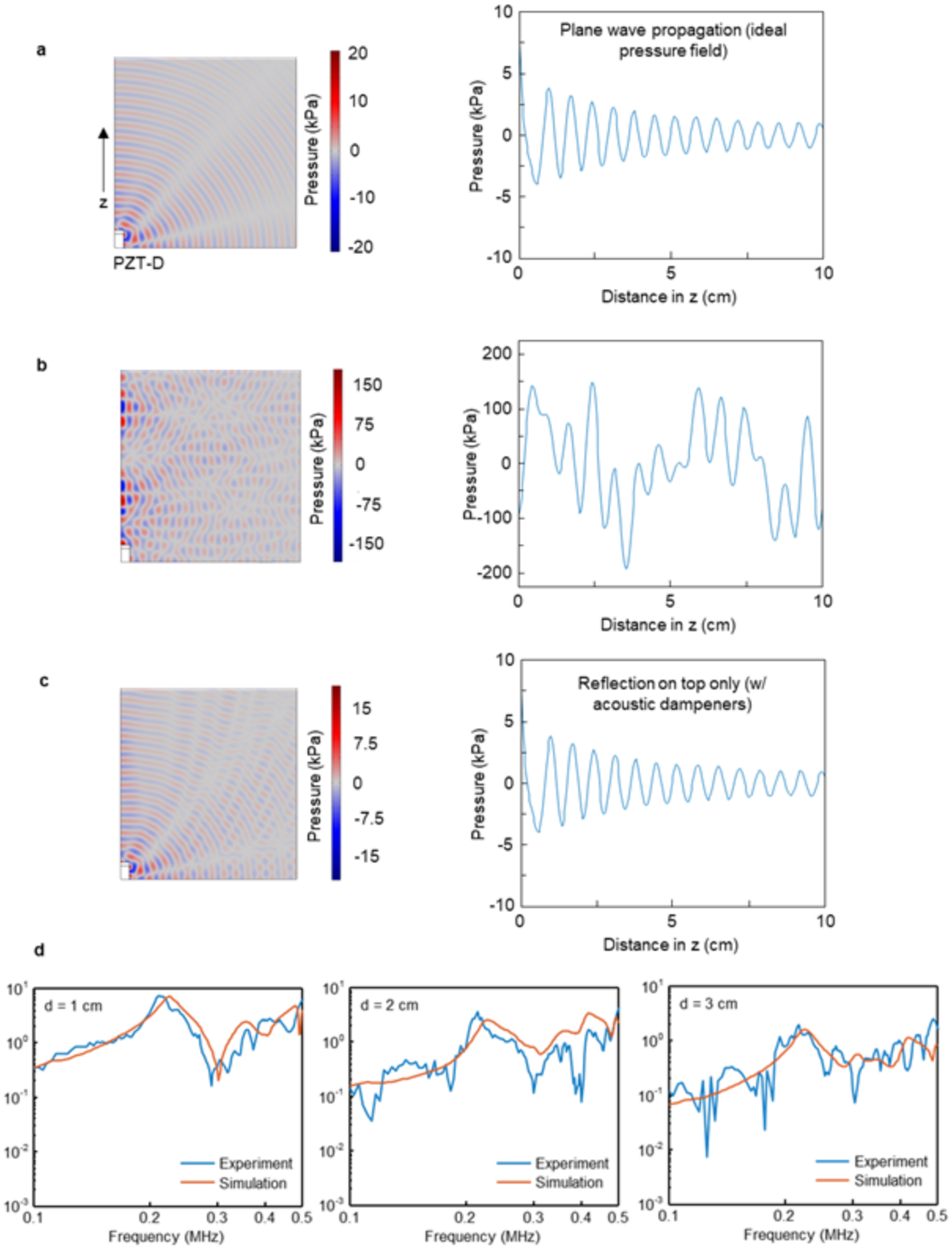

Figure 12 Impact of water-tank dimensions, reflections and need for acoustic dampers. 2D axis-symmetric acoustic pressure distribution in water (left side) and along the z-axis through the center of

the PZT-D (right side) for **a,** ideal boundary conditions with no reflections, **b,** reflective water-air boundary on top and water-glass-air side-walls and **c,** reflective water-air boundary on top, and acoustically damped side-walls. **d,** Experimentally measured (blue) and simulated (red) frequency-sweep plots (100 kHz - 500 kHz) for pressure at distance of 1, 2 and 3 cm along the z-axis.

The pressure results are evaluated by comparing the experimental and simulated pressure results across different distances from the surface of the device. In this study, we are interested in the investigation of the resonant frequency in the lower frequency range of 220 kHz, since the cavitation thresholds are lower at this frequency range. **Fig. 12d** shows the pressure results at the distance of 1 cm, 2 cm, and 3 cm away from the surface of the device in water. The results show that the resonant frequency is independent of the location of measurement in the water tank as the distance increases from the surface of the device: however, the pressure amplitude and the fluctuations of the experimental results are affected. The pressure at the resonant frequencies decreases from 9 kPa to 3 kPa and 2 kPa as the hydrophone is moved from 1 cm to 2 cm and 3 cm away from the surface of the device for a driving voltage of 10 V_{pp}. At distances closer than 1 cm from the surface of the piezoelectric disk transducer, it was not possible to make near-field experimental measurements.

Despite the simplicity of the FEA model, the simulation results match the results of the experiments that were conducted in terms of efficient description of the resonant frequency and amplitude of pressure. However, there is some discrepancy in terms of disturbances in the pressure waveform. The likely explanation for this discrepancy is attributed to the fact that electromagnetic wave coupling is present in the experimental measurement. This coupling effect results in many disturbances even after filtering out the undesirable frequencies in the obtained signal via a low pass filter. The

fluctuations could be caused by alignment issues and the distortions of the hydrophone. Furthermore, because we are employing a bare piezoelectric disc without any backing layer, the transducer exhibits a significant amount of ringing. The variation in amplitude between the FEA model and experiment is also a result of the wave interference caused by this ringing. Nonetheless, the FEA model remains a useful tool for initial approximation of acoustic pressure.

2.2.2. Pressure-voltage relations in far-field

Next, we investigate the influence of applied voltage on the acoustic pressure. We vary the applied voltage to the transducer and measure the acoustic pressure using a hydrophone at a constant frequency of f_r and a constant distance of 1 cm between the device and the hydrophone. As the applied voltage is changed from 45 to 100 V, the output acoustic pressure value increases from 51.3 to 116.4 kPa, maintaining a linear relationship (**Fig. 13a**). Overall, there is excellent agreement between the experimental and simulated absolute pressure values for the far-field measurements at different driving voltages. This allows a confident extrapolation of pressure values at 50 V using the FEM model for the pressure field within 1 cm of the PZT-D surface.

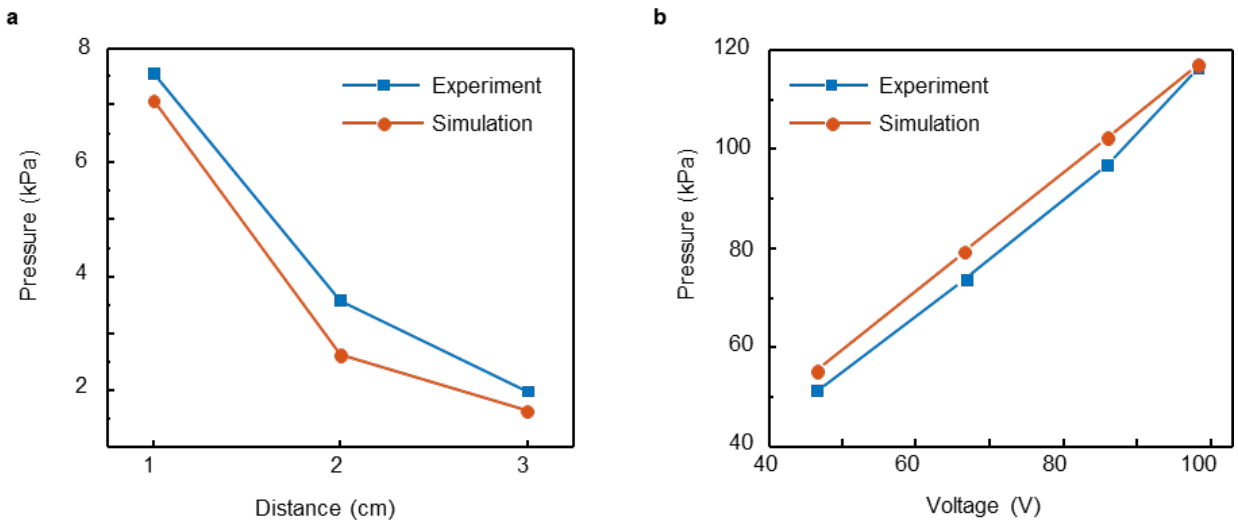

Figure 13 **Acoustic pressure characterization of the device inside a water tank. a,** Experimental measurement and numerical simulation results of acoustic pressure at f_r at different distances away from the device along the z-axis at 10 V peak-to-peak. **b,** Experimental measurement and numerical simulation results of acoustic pressure under different applied voltages at f_r 1 cm away from the surface of the device in the water.

2.2.3. Pressure-frequency relations in near field

Fig. 14 shows the 2D contours of the acoustic pressure distribution in water in the vicinity of the device at the two resonance modes. The results indicate the specific areas of the water that exhibit the highest acoustic pressure. The pattern and magnitude of the acoustic pressure distribution are distinctly different for the two main modes of vibration. For radial extension, the wave propagation in the water has a wide central lobe with the maximum pressure of ~100 kPa occurring near the middle of the PZT-D. In thickness deflection, the maximum pressure of 450 kPa occurs within a narrow axial band directly above the center of the PZT-D and fluctuates significantly with an eventual drop-off towards the edges. **Appendix A2** show the damping of

pressure while moving outwards from the center of the PZT-D surface radially (r = 0) to the edge (r = 5 mm), and in the z-direction (z = 0) to the water surface (z = 10 mm).

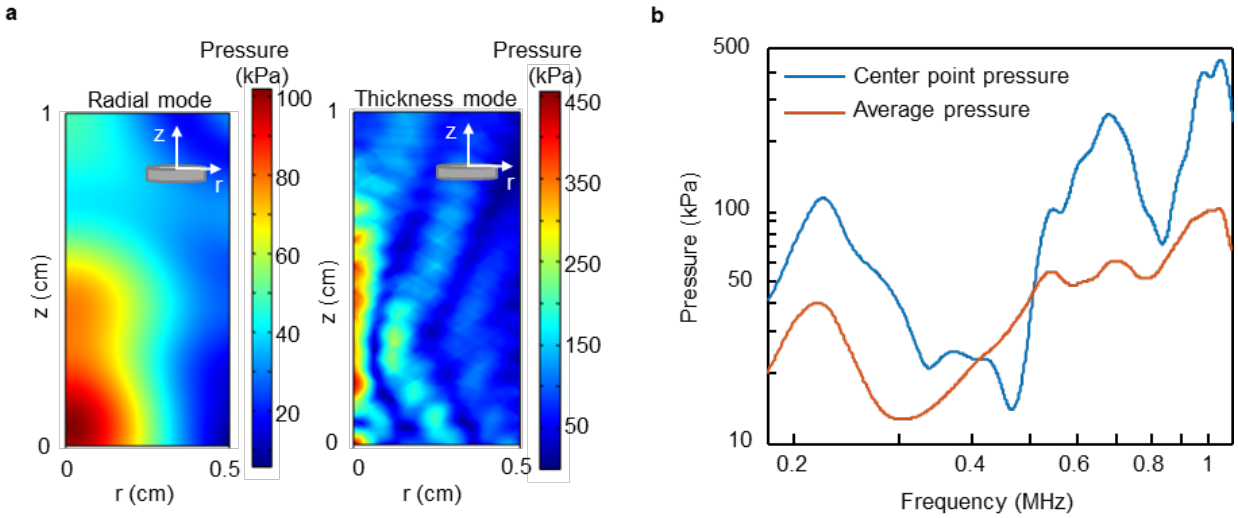

Figure 14 Simulated acoustic pressure in near-field for **a,** radial (left) and thickness (right) mode. **b,** spatially averaged pressure for a 1-mm thick slice above the transducer

Further, we evaluate the pressure field for the two resonant modes to determine the operating frequency for the system (**Fig.14b**). Despite the occurrence of a higher peak pressure at 1 MHz, the spatial average of the pressure over a volumetric slice of 1 mm thickness over the top-surface of the PZT-D is more comparable for the radial mode and thickness mode as shown in **Fig. 14b**. The cavitation threshold depends not only on the acoustic pressure but also on the irradiation time, and is thus typically lower for larger cycle times or lower frequencies [29], [38]. It has been experimentally verified that the cavitation threshold at f_t is almost double of that at f_r [37] which is also observed by performing high-speed videography of the cavitation regime. Bubbles are nucleated at a threshold voltage of 50 V at the radial mode frequency (f_r). However, no bubbles are formed at this voltage when the device is operated at the thickness mode frequency (f_t). If the frequency is immediately

switched from f_r to f_t, the streaming bubbles nucleated at the lower frequency come to a sudden standstill and oscillate in place **(Supplementary Video S5**). Therefore, the first radial mode of resonance (f_r) is selected for the operation of the device going forward to maximize both convective effects due to acoustic streaming as well as inertial cavitation events at a low threshold voltage.

2.2.4. Impact of device geometry on the pressure field

Up to this point, the scope of modeling of the conformable ultrasound face patch was limited to a single element. However, achieving drug delivery across an entire region such as the cheek or forehead demands a conformable patch with 2D arrangement of elements. The effect of skin, the encapsulating polymer and any interaction or coupling between the PZT-D elements is subsequently investigated.

Fig. 15a-c illustrates the 3D view and 2D cross sectional view of array elements of the ultrasound patch used in our FEM simulations for modeling the *in vivo* trials when the device is adhered to facial skin. The geometry is composed of 4 PZT-Ds arranged in a 2x2 configuration and encapsulated in a soft PDMS substrate with a total thickness of 4 mm. Circular cavities of 6 mm radius and 3 mm depth are patterned concentrically around the PZT-D elements in the PDMS substrate. The cavity is filled with the drug solution, and it acts as a drug reservoir while providing a controlled space for cavitation action of bubbles against the skin surface. The PZT-Ds are driven in parallel with a sinusoidal voltage of 50 V_{pp}.

Several features are of interest within the 2D array of the transducers. First, to study the impact of PZT-D spacing, a simplified configuration is considered wherein the PZT-Ds are arranged on a flat PDMS substrate without the patterned cavities (**Fig. 15a**). A 2 mm layer of skin is applied at a separation distance of 1 mm from the top surface of the PZT-Ds. The cross-section through a set of 2 PZT-Ds is taken to generate the pressure maps (**Fig. 15b**).

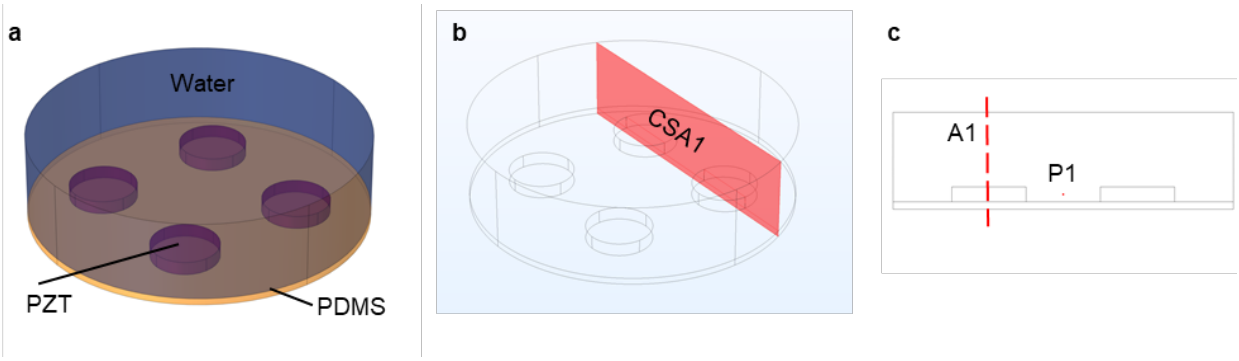

Figure 15 **a,** Simplified arrangement of 2x2 array of PZT-D elements on a 1-mm thick PDMS substrate. **b,** Cross-section considered across two PZT-D elements for the pressure maps. **c,** Axis A1 through the center of the PZT-D element, and point P1 between 2 PZT-D elements, positioned 1 mm from the top of the PDMS substrate.

3 PZT-D separation distances are considered - 10 mm, 4 mm and 2 mm as shown in **Fig. 16** and examined across plane CSA1 as shown in Fig. **15b**. Peak pressures of ~180 kPa are generated within the fluid medium in all 3 configurations, showing that it is possible to generate pressures larger than the cavitation threshold (~100 kPa) in all three cases. The main lobes of peak pressures are contained within a small region directly above the center of each PZT-D at all separation distances. As the PZT-Ds get closer, the side lobes of pressure from each PZT-D element generate patterns of constructive interference, creating spikes in pressure and increasing the total area within the fluid conducive to the nucleation of cavitation.

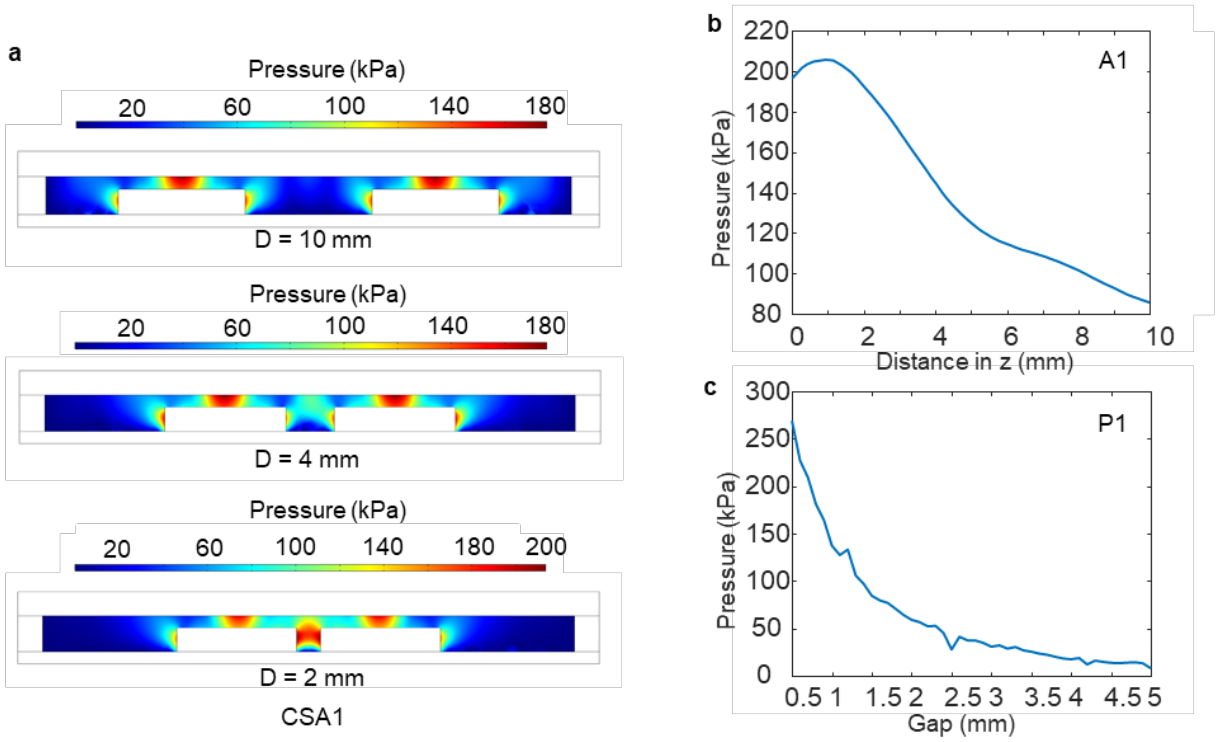

Figure 16 Simulated acoustic pressure distribution within the cUSP 2D array. **a,** Pressure distribution in fluid coupling medium for CSA1 for different PZT-D separation distances (10 mm, 4 mm and 2 mm, top to bottom). **b,** Pressure profiles along axis A1, starting at the surface of the PZT-D element. **c,** Pressure profile at point P1 for different separation gaps between the PZT-D elements.

As a quantitative indicator of this effect, the peak pressure is plotted at a point P1 directly between 2 PZT-Ds (**Fig. 16b,c**). The pressure at P1 drops to 50% of its peak value at around 3 mm separation. This provides a good directive to design the PZT-Ds as close to each other as possible without compromising the mechanical stability of the patch. The variation in absolute pressure along the z direction above the center of the PZT-D in an array is demonstrated in **Fig. 16c**. The pressure drops off steeply below the cavitation threshold when the distance in z is larger than 1.5 mm, and it is thus desirable to position the skin within this distance.

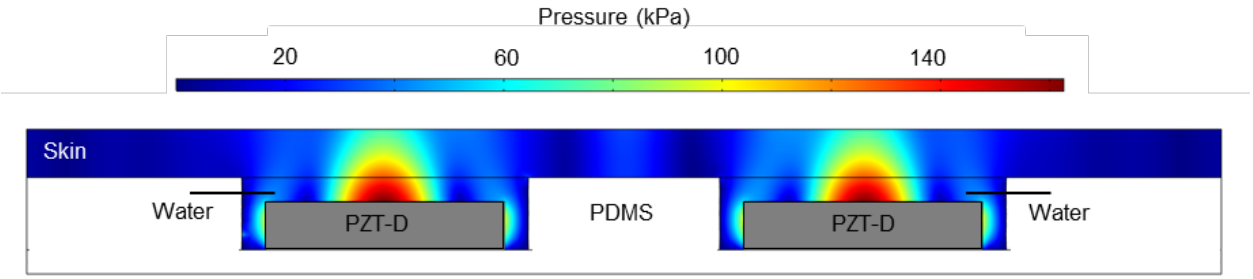

Figure 17 Simulated acoustic pressure distribution in the water cavity and skin shown in cross-section of the cUSP device taken diametrically through the center of 2 PZT-Ds.

The final configuration of the patch with 10 mm PZT-D spacing and structural PDMS cavities placed against the skin is shown in **Fig. 17**. The pressure in both the fluid coupling medium and the skin is plotted in a continuum. There is minimal distortion in the pressure field at the water-skin interface, which is expected as the acoustic impedances of the two materials are similar at 1.48 MRayl and ~1.6 MRayl respectively. However, there is some degree of reflection of ultrasound energy both from the skin as well as the PDMS walls in the cavity, which creates a zone of constructive interference close to the top surface and sides of the PZT-D, and causes a spike in the peak pressure to 140-160 kPa, as compared to the peak pressure of 100 kPa observed for the case of a bare PZT-D in a water column as shown in **Fig. 14a**. The side lobes of pressure are suppressed due to the structural PDMS columns between the PZT-D elements. In future iterations of the design, it is desirable to reduce the size and thickness of the PDMS columns to facilitate constructive interferences of the side lobe pressures and increase the likelihood of cavitation. These simulations demonstrate that for the given 2D-array patch configuration, the pressure fields are well-contained above each PZT-D element, and the geometry of the PDMS cavity and application of the device against skin in fact serves to compound the peak acoustic

pressures beyond the cavitation threshold. Further, it is shown that the distance between the piezoelectric elements can have a certain degree of influence on the acoustic pressure distribution, but undamped pressure zones in excess of ~140 kPa are formed within the medium in all configurations of the patch.

2.3. Cavitation detection

2.3.1. Ultrasubharmonic and broadband noise characterisation

We proceed to studying the bubble dynamics induced by the PZT-D system. In this experimental study, the onset and intensity of cavitation is first characterized by measuring the subharmonic response of the acoustic pressure field in the fluid medium. Through simultaneous collection of spectroscopic and acoustic data, Johnston demonstrated a clear correlation of bubble radius and shockwave period with the measured acoustic signal as a subharmonic of the driving frequency [58]. An increase in broadband noise and subharmonic signal strength are representative of inertial cavitation and the emission of pressure shockwaves [29], [59]. A needle hydrophone (HNC-0400, Onda Corp.) placed close to the PZT-D is used to measure the subharmonic component of the acoustic field due to cavitation. The hydrophone is positioned perpendicular and out of the direct field of oscillation of the PZT-D to reduce the amplitude of direct vibrations from the PZT-D and allow pick-up of small signals of the cavitation field, which can be assumed to be spherically symmetric.

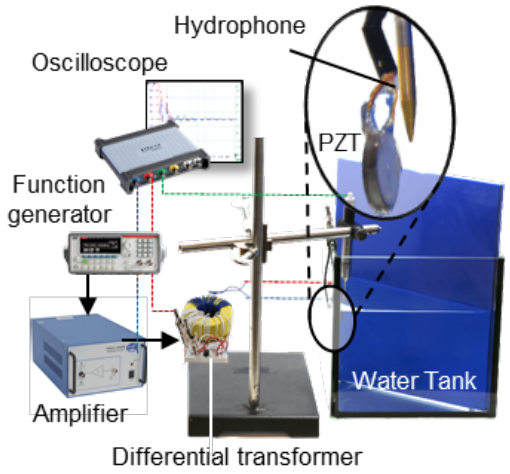

Figure 18 Experimental setup for cavitation detection. Acoustic absorbers (blue) were placed on the four side walls of the water tank to avoid reflection of ultrasound waves from the walls. Inset shows the magnified view of the relative orientation of the hydrophone and the PZT-D.

Fig. 18 shows a schematic representation of the cavitation measurement setup driven at the radial mode. The threshold voltage for cavitation is determined by gradually increasing the driving voltage until a subharmonic (f/2) or ultra-subharmonic (3f/2) signal occurs in the Fast Fourier transform (FFT) spectrum of the hydrophone output signal that is significantly higher than the noise floor **(Fig. 19**).

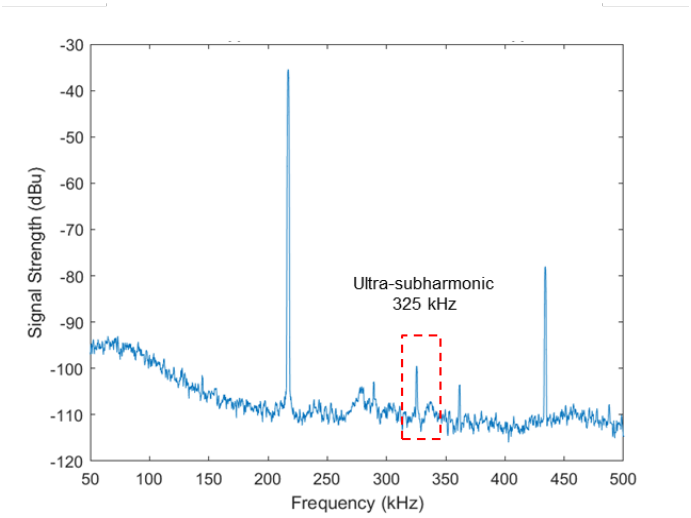

Figure 19 Appearance of ultrasubharmonic peak (3f/2, 325 kHz) in the acoustic pressure spectrum at 50 V.

The ultra-subharmonic signal appears first, which is attributed to the fact that the sensitivity of the hydrophone is higher in this frequency range. The ultra-subharmonic signal and broadband noise are obtained by averaging 32 frames of FFT spectrum for 3 different devices. As seen in **Fig. 20**, the magnitude of the ultra-subharmonic peak increases almost linearly with increasing voltage.

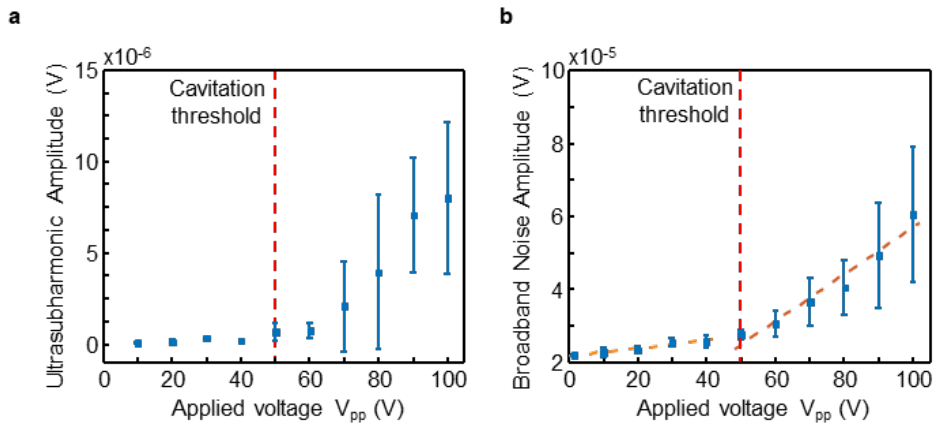

Figure 20 Increase in signal strength of ultra subharmonic and averaged broadband noise with increasing voltage.

The standard deviation in the ultra-subharmonic signal magnitude starts increasing significantly when the applied voltage is 50 V and above, indicating sporadic appearance of ultra-subharmonic peaks. Given the stochastic nature of inertial cavitation, its dependence on existing bubble nuclei populations [60], and short lifetime of inertial bubbles [61], we see large variations in the measured ultra-subharmonic signal even over a long sampling duration (averaged over 32 frames, corresponding to a total sampling period of 1.6 ms (see **Appendix B2**)). However, since the total 'on-time' for each ultrasound pulse for the final system (~50 ms) is far greater than this sampling period, there is a much greater likelihood of obtaining inertial cavitation action for a significant portion of the application time. Thus, we refer to the acoustic pressure generated when the applied voltage is 50 V as the cavitation threshold, which corresponds to around 95 kPa. At an applied voltage of 90 V and above, the data becomes significantly different ($p < 0.05$) from that of 10 V, implying more frequent cavitation events occurring every frame. Similarly, the broadband noise magnitude increases almost linearly with increasing voltage (**Fig. 2.18b**), and there is

a 6-fold increase in slope after crossing the cavitation threshold of 50 V (from 1.06 x 10^{-8} to 6.42 x 10^{-8}). This suggests a higher count of bubbles and/or more violent bubble collapses at higher voltages.

The large standard deviation in the ultra-subharmonic data can be attributed to several factors in the experimental setup. The experiment is carried out with 3 different devices which may have minor differences in coating thickness and distribution across the body of the PZT-D, impacting the pressure profile in the water surrounding the PZT-D. Further, the total dissolved gas in the water changes with time, which influences the initial nucleation seeds available for the onset of cavitation. The FEM results presented in **Fig. 9** indicate that it is less likely that the large standard deviations stem from varying coating thicknesses, as even a 1-mm thick polymeric backing has negligible impact on the PZT-D displacements and the coating thickness used in the studies is significantly smaller than this value (< 100 μm, **Appendix A1**). The dependency and variation with total dissolved gas should thus be carefully reduced by incorporating pre-existing nucleation seeds in the coupling medium for future embodiments of the system. Despite these discrepancies, the overall observed trend with the data across the 3 devices uniformly increases with increasing voltage.

2.3.2. High-speed imaging

High-speed videography (Phantom v2512, Vision Research Inc.) is performed to provide further insight into the cavitation regime in the vicinity of the PZT-D. This reveals that indeed a larger number of bubbles at higher streaming speeds are generated as the voltage is increased, as seen in **Fig. 21a-b** and **Supplementary**

Video S3, S4. ImageJ is used to threshold the images and count the average number of bubbles across a stack of frames (see **Appendix B2**). The bubble count and streaming speed increase by 149% and 144% respectively as the voltage is ramped from 50 V to 100 V. Correspondingly, a 15 dB increase in ultra-subharmonic signal strength is obtained for the same voltage gain. We expect bubble nucleation at the locations of maximum pressure above the PZT-D as predicted by the simulated pressure maps in **Fig. 14a**.

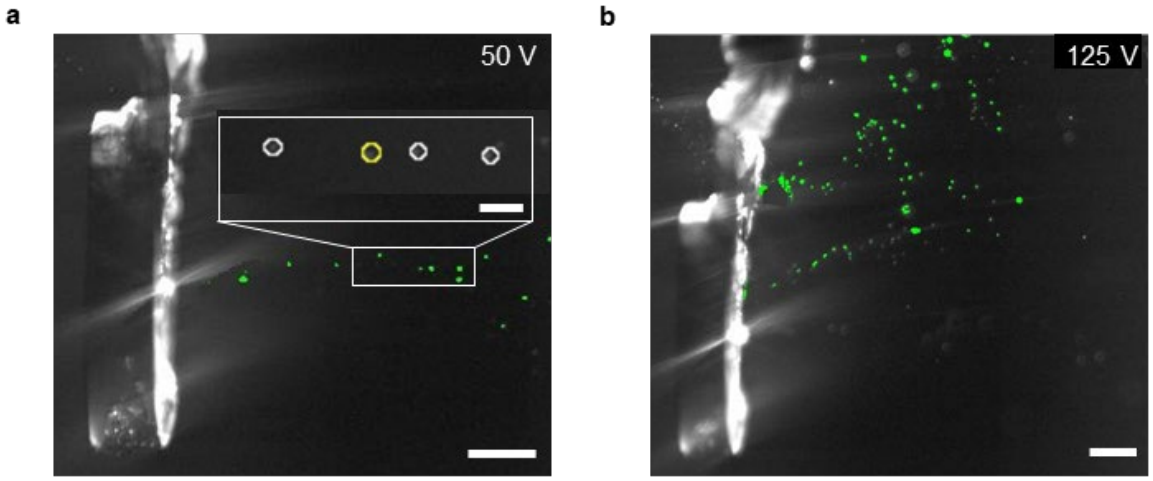

Figure 21 **a,** Still images from high-speed camera footage when the PZT-D was driven at 50V underwater, showing a streamline of bubbles originating from the center of the PZT-D; Scale bar, 2 mm. Inset shows the zoomed in view of bubbles (the average bubble radius was 50-70 μm). Scale bar, 200 μm. **b,** Still images from high-speed camera footage when the PZT-D was driven at 125 V, showing a larger volume of streaming bubbles at higher voltage at both center and edge of the device. Scale bar, 2 mm. The corresponding videos are attached in **Supplementary Videos. S3, S4**.

In radial mode, this corresponds to the center of the top surface and the side-walls of the PZT-D, and indeed a stream of bubbles can be seen originating from both these locations in **Fig. 21b** and **Supplementary Video S4**. The relation between the

applied voltage as ultrasound pulse and the measured acoustic pressure maintains linearity up to 120 V, and no step change in the pressure field is observed. This suggests that the generated bubbles are continuously streaming and do not accumulate in a given region to create a pressure dampening effect as seen with larger bubble clouds [53].

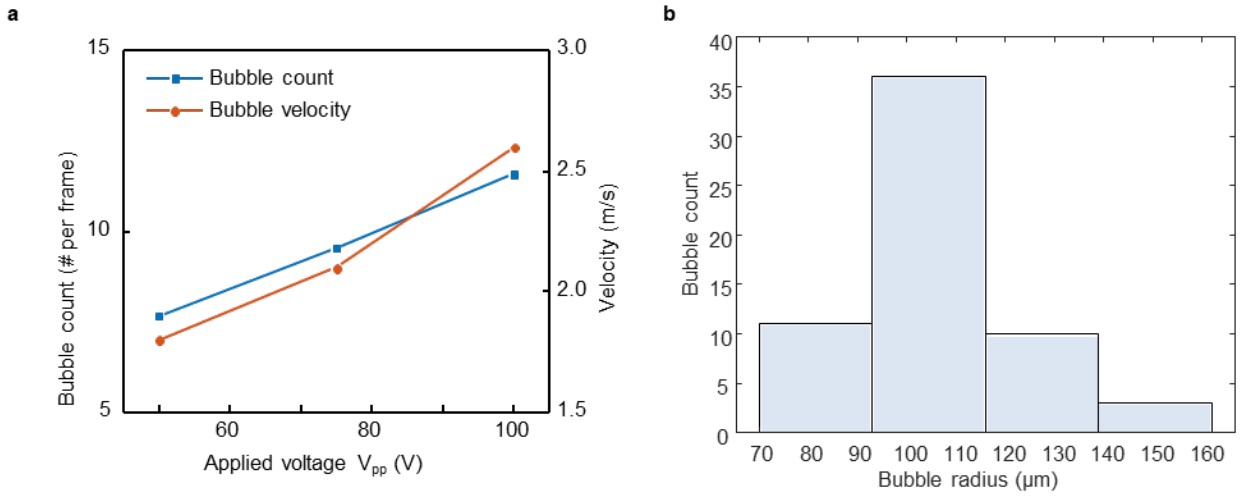

Figure 22 **a,** Bubble count and bubble velocity as a function of applied voltage. In all cases, the PZT-D was driven in radial mode (f_r). **b,** Histogram showing distribution of the radii of selected bubbles.

After identifying the bubble nucleation zone, 2 teleconverters are used to image the bubbles at a higher magnification (4X). The bubble radius is characterized from these images and is found to be in the range of ~95-115 μm. A histogram of the distribution of the bubble radii is presented in **Fig. 22**. The anticipated bubble size at f_r is ~15 μm from the well-known relation between frequency and bubble radius (f (kHz) x R (μm) = 3000) [30], [62]. However, after nucleation, the bubbles coalesce and grow within a few energy cycles and often the measured bubble size is significantly larger than the theoretically predicted bubble size [63], [64]. This is a feasible assumption

given that a maximum frame rate of the imaging setup is 10,000 fps, and the cycle length of the applied ultrasound is around 20 times smaller than this value.

The phenomena observed above confirm a repeatable onset of inertial cavitation within the medium above a threshold voltage of 50 V. While the above characterizations have been performed on a single PZT-D element, the results are largely representative of the cavitation action expected in the 2D array patch. For future embodiments with closer packing of PZT-Ds, it would be beneficial to study the cavitation dynamics directly within the patch to account for any constructive/destructive interferences in the pressure fields generated by each element.

2.4. *In vitro* drug permeation studies

2.4.1. Experimental setup of a Franz cell

In order to evaluate the efficacy of the PZT-D as a sonophoresis device, a permeation study is performed on a porcine model *in vitro* to evaluate NIA transport in a Franz diffusion cell. A number of studies have prescribed a well-developed protocol to assess the extent of diffusion using high-performance liquid chromatography (HPLC), tape-stripping (TS) and confocal raman spectroscopy (CRS) and demonstrated correlations between the various methods [50], [65], [66]. The *in vitro* permeation setup is shown in **Fig. 23**, and details of the process are provided in the **Appendix B3**.

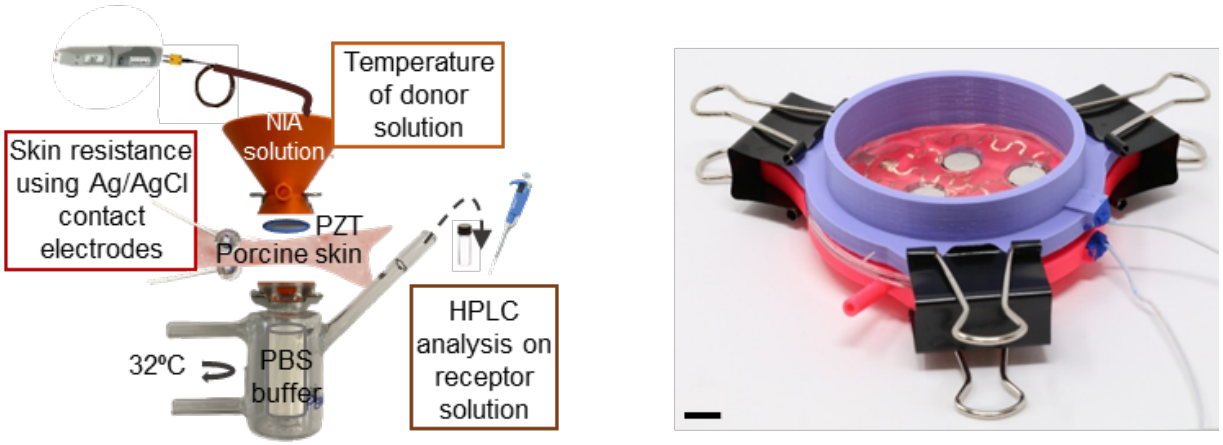

Figure 23 Franz cell setup for single-element PZT-D (left) and 2D array cUSP (right)

A 3% weight/weight (w/w) solution of NIA in phosphate-buffered saline (PBS) is used as the drug formulation. The choice of PBS as the solvent is guided by an

experimental study comparing the cavitation threshold for different solvents. Among the formulations of PBS, glycerol, and propane-1-2-diol, PBS displayed the least viscous damping and minimum cavitation threshold (**Appendix A3**). The porcine skin is actively treated with the PZT-D for 10 minutes within the cell at 32 °C with the drug formulation in the donor chamber and PBS in the receptor chamber. The PZT-D is maintained at a distance of < 2 mm from the surface of the skin using positioning rods in the Franz cell. To monitor the diffusion process, the concentration of the receptor solution is sampled at fixed time intervals throughout a 1-hour period while the skin resistance is simultaneously measured using in-cell integrated Ag/AgCl electrodes. As a control, the same study is set up to allow passive penetration of the solution across the skin without the application of ultrasound.

2.4.2. Permeation profiles with single elements

We anticipate heat generation in the cell due to dissipation of a portion of the applied ultrasound energy in the fluid medium and the tissue. An initial assessment with an infrared thermal camera revealed that the temperature of the solution in the Franz cell rises significantly above room temperature. (**Fig. 23b**). An in-depth study was subsequently conducted using a calibrated commercial thermocouple logger to measure the temperature profile of the solution in the donor chamber using a PBS solution and PDMS membrane to simulate the skin. In this case, a temperature rise of 1.1 ℃ $minute^{-1}$ was recorded when a 100% duty cycle was applied. Based on previous literature, applying a smaller duty cycle is often preferred in order to provide a cool-down time for the ultrasound transducer and control the heat produced within the

system [67]–[69]. **Fig. 23** shows the details of the thermal investigation and **Table 2** lists the temperature rise associated with various duty cycles.

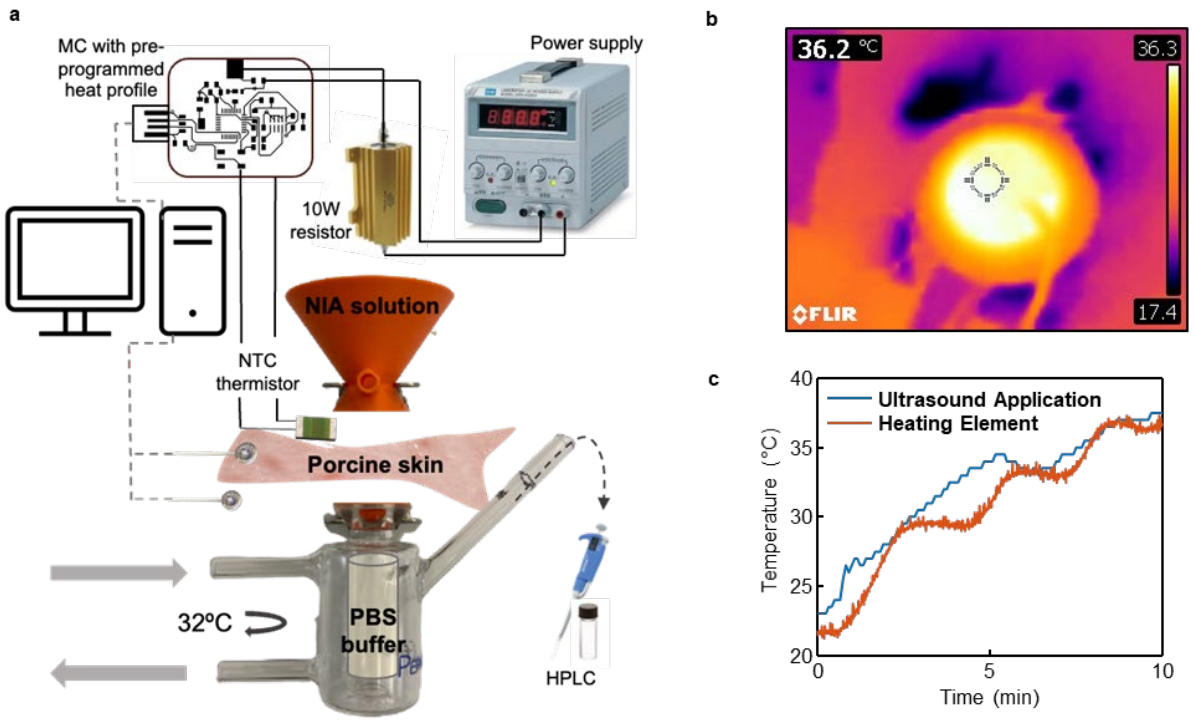

Figure 24 **a,** Schematic of the experimental setup for thermal control study in Franz Cell. **b,** Image with infrared camera reveals that solution temperature in Franz Cell with ultrasound is significantly higher than room temperature. The colormap is in units of Celsius. **c,** Overlay of the heat profile generated by the pre-programmed heating element and that measured in the case of the PZT-D

Medium	Duty Cycle (ON%)	# of ON Cycles	Temperature rise/min (℃)
PDMS/PBS	100%	N/A	1.1

PDMS/PBS	25%	5000	0.3
PDMS/PBS	50%	2500	0.35
PDMS/PBS	50%	5000	0.45
Porcine Skin/PBS	50%	5000	1.5

Table 2 Temperature rise in Franz cell with various duty cycles

While a small duty cycle is desirable from a heating perspective, the ON period should be sufficiently long to allow the nucleation, growth and collapse of bubbles to take place. A 50% duty cycle with 5000 ON cycles was deemed a reasonable compromise, and was further validated in the Franz cell with the porcine skin. A total local temperature rise of 15 °C over 10 minutes is measured. The average skin temperature is 32 ℃ (91 ℉), which maps to a maximum temperature of 47 ℃ after 10 minutes of ultrasound. While this rise in temperature is significant, there are multiple approaches to mitigate this effect, which are presented subsequently in **Section 3**.

However, from the perspective of experimental control, it is important to characterize the permeation enhancement provided by the ultrasound as distinct from that provided by the application of heat. A thermal control study is designed and performed using a microcontroller and a resistive heating element to mimic the thermal ramp observed with the ultrasound transducer.

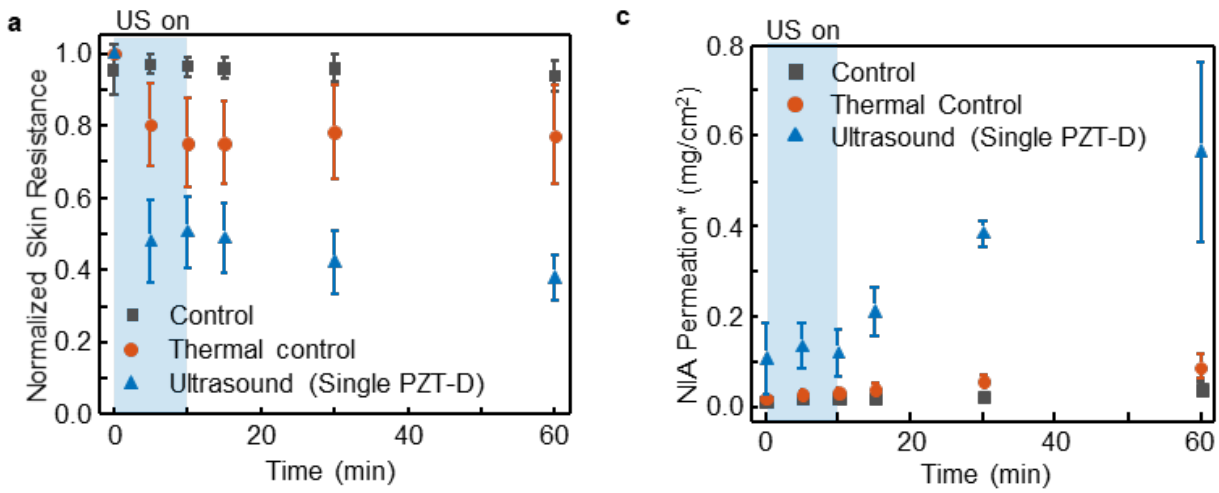

Figure 25 Variation in skin resistance and permeation enhancement with a single element PZT-D. **a,** Normalized skin resistance with application time of ultrasound and heat (thermal control) versus control (passive permeation) for a single PZT-D. Error bars represent the standard deviation of the measurements (n = 3). **b,** Amount of niacinamide (NIA) permeated with the application of ultrasound and heat (thermal control) versus control (passive permeation) for a single PZT-D element. Error bars represent the standard deviation of the measurements (n = 3).

The trend of skin resistance and amount of NIA permeation from the in-vitro permeation study with a single PZT-D element are shown in **Fig. 24a** respectively for 10-minute ultrasound, thermal control (10-minute heat), and passive control. From t = 5 min onwards, the permeation amount of samples treated with ultrasound is significantly different from that of the passive control samples, while the permeation amount of thermal control samples do not show a significant difference compared to that of passive control for the whole duration of permeation monitoring. The samples treated with ultrasound show a 19.2-fold increase in permeability as compared to the passive control at the end of 60 minutes (**Fig. 24b**). Application of heat provides a 2.2-fold increase in permeability as compared to the passive control, which indicates that the acoustic streaming and cavitation accounts for a significant part of the enhancement mechanism provided by the sonophoresis device. The total dose delivered in each case is calculated using a calibration curve shown in **Appendix A4**.

The absolute dose delivered in a 1-hour period is 0.68±0.20 mg/cm^2. This dosage is significantly higher than that obtained with a previous study under pseudo-infinite dose conditions with full-thickness skin wherein negligible permeation was observed within the first 4 hours [70]. High NIA transport (0.20-0.80 mg/cm^2) in a 1-hour period in observed in passive diffusion studies with synthetic membranes [65], [70], but this can be attributed to the smaller thickness (7-160 μm) and tailored physicochemical and pharmacokinetic properties of these membranes as compared to the highly heterogeneous 2-3 mm thick porcine skin. It must also be noted that a smaller enhancement may be observed with human skin [70].

The skin resistance decreases with application of both ultrasound as well as heat, with a larger decrease observed in the case of ultrasound application. While the results are normalized with the initial skin resistance value, large standard deviations are still observed in the skin resistance data (**Fig. 24a**). This can be attributed to the bio-variability of the specimens. The overall thickness of the samples, relative composition of fat to dermal tissue, presence of small hairs and lesions on the skin samples all impact the resistance value measured across the skin sample. However, the 3 test cases (10 minute ultrasound, 10 minute heat and passive control) each occupy distinct ranges with almost no overlap. On average, the skin resistance after 60 minutes decreases by 6.3% in the case of passive control, 22.7% in the case of heat application and 62.3% in the case of ultrasound.

2.4.3. Permeations profiles with a two-dimensional array of actuators

As a final step to test the device efficacy, we perform a skin permeation study with the 2D array patch in a custom Franz cell. The patch was laid flat on the skin and the donor NIA solution was added to completely fill the cavities around the PZT-Ds and until the patch was just submerged to ensure no trapping of air bubbles in the fluid reservoir. The treatment protocol was identical to the single-element study, and the permeation profile was monitored for 1 hour. Considering that heat application accounts for a relatively small amount of the overall permeation enhancement resulting from ultrasound, thermal control was not conducted for this series of 2D array permeation experiments.

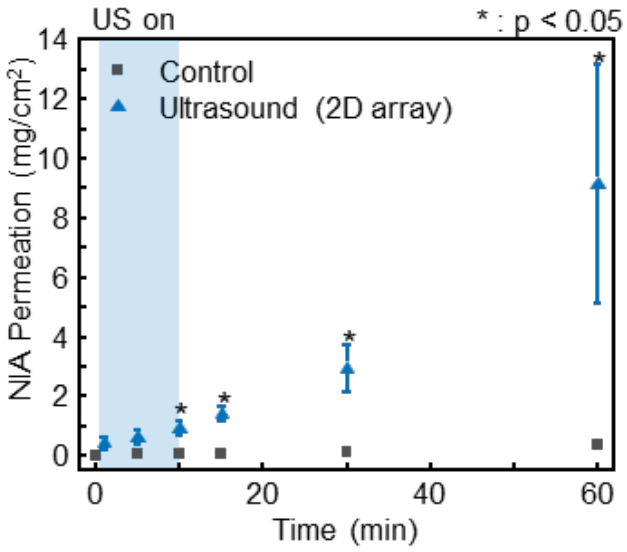

Figure 26 Amount of NIA permeated with application of ultrasound versus control (passive permeation) for the cUSP array. *Indicates that the data set is significantly different from the control ($p < 0.05$). †Indicates that the skin area considered for the calculation has been adjusted to equally discount the neighborhood of skin left uncovered for each study (see **Appendix B4**). For all cases, ultrasound is applied for 10 minutes (blue shaded region)

The cumulative amount of NIA permeation from the in-vitro permeation study with the cUSP array is shown in **Fig. 25** for 10-minute ultrasound and passive control.

From t = 10 min onwards, the permeation amount of samples treated with ultrasound is significantly different from that of the passive control samples. The cumulative dose delivered in a 1-hour period is 0.35±0.09 mg/cm^2 for control (passive permeation) and 9.14±4.00 mg/cm^2 for ultrasound application with the cUSP. The samples treated with ultrasound show a 26.2-fold increase in permeability as compared to the passive control at the end of 60 minutes. Since the primary mechanism responsible for the permeation enhancement is inertial cavitation, we expect the effect to be highly localized around the PZT-D. The skin area is adjusted to discount the area of the untreated skin in both setups (see **Appendix B4**). In the single element study, the PZT-D covers 25% of the skin directly exposed to the ultrasonic field, while only 12.3% of the total skin area is covered by the 4 PZT-D elements in the larger Franz cell (Supplementary Fig. S10a). Once the results have been compensated for treated vs. untreated skin regions, the enhancement ratios obtained at the end of 1 hour with the patch and with the single element are comparable at 26.2-fold and 19.2-fold respectively (**Fig. 24b**). The higher enhancement ratio provided by the cUSP can be attributed to the larger acoustic pressure generated within the PDMS-bounded cavity walls. We therefore demonstrate the feasibility of the patch design and the PDMS encapsulation in allowing undamped application of ultrasound energy to the skin over larger areas in a conformal, unobtrusive form factor.

2.4.4. Comparison with microneedles

To explore how our IFS device performs compared to other permeation enhancement techniques, we conducted in vitro drug permeation studies with microneedling treatment, which is the most common and widely accessible

transdermal permeation enhancement method. The porcine skin was pre-treated with a commercial derma roller (200 μm length) and the NIA permeation profile was monitored for up to 6 hours. The cumulative amount of NIA permeation from the in-vitro permeation study with the cUSP and microneedle are shown in **Fig. 26**. From t = 10 min onwards, the NIA permeation of samples treated with ultrasound is significantly different from that of the passive control samples, while that of the samples treated with microneedle remain similar to that of the control throughout the 1-hr permeation monitoring period. The cumulative dose delivered in a 1-hour period is 4.00 mg/cm^2 for microneedle treatment and 9.14±4.00 mg/cm^2 for ultrasound application with the cUSP. The results show that a 10-minute ultrasound application with the cUSP is able to deliver 20.8-fold of NIA into the skin compared to microneedling treatment in a 1-hour period, and the drug permeation enhancement may continue to increase over time.

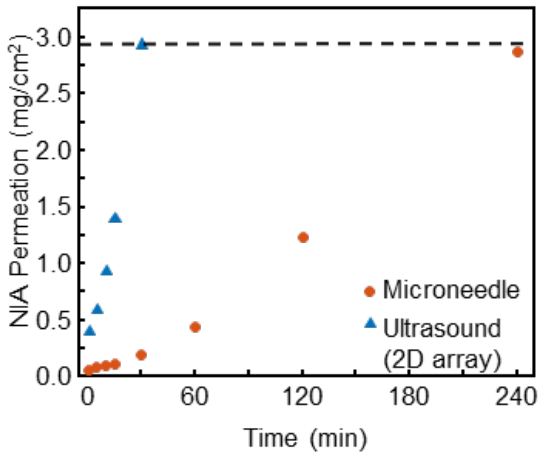

Figure 27 Amount of NIA permeated with application of ultrasound versus microneedles. The cUSP array achieves similar NIA permeation within 30 minutes as compared to the 4-hour diffusion curve with microneedles.

From **Fig. 27**, we observe that the cumulative dosage obtained with ultrasound treatment at t = 30 min (2.94 mg/cm^2) can only be achieved with microneedle treatment at a much later time point, t = 240 min (2.88 mg/cm^2). The permeation rate resulting from ultrasound application is approximately 13.2 times larger compared to that with microneedle treatment (slope of 0.15 and 0.01 mg/cm^2·min^{-1}, respectively). We therefore demonstrate the superior drug permeation enhancement provided by ultrasound treatment with the cUSP as compared to other permeation enhancement techniques.

2.4.5. Dye penetration studies

As the fate of the drug under consideration is in the skin itself (within the viable epidermis and dermis layer), we further performed a short study to ensure successful retention of the drug within these layers. 1 cm^2 pieces of pig skin were fixed in a diffusion cell with 0.75 ml of standard stock solution (1 mg/ml in PBS) of Rhodamine B in the top chamber, and PBS in the bottom chamber to maintain skin hydration (**Fig. 28**)

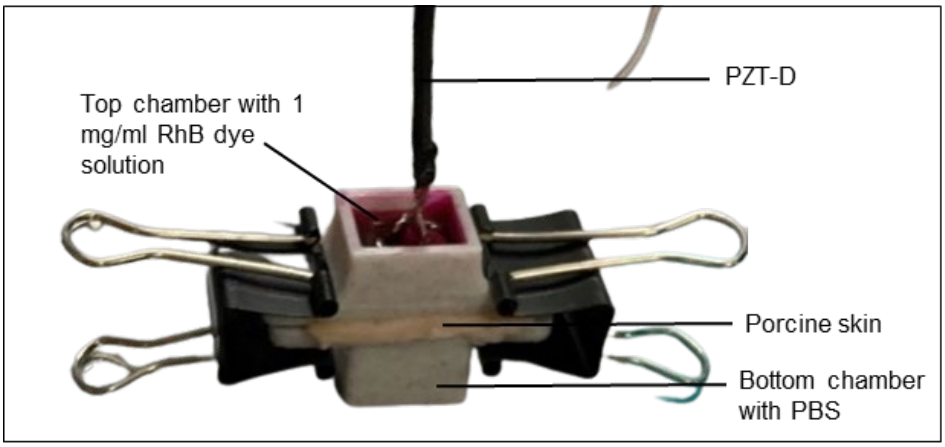

Figure 28 Dye permeation study setup

The same ultrasound treatment was applied at 50 V, 50 % duty cycle for a 10-minute duration. The cells were allowed to stand for 24 hours at 32℃. A cross-section of the skin was analyzed using a multi-photon confocal microscope. Details of the study, histology and imaging protocols are given in **Appendix B5**. **Fig. 29** shows the fluorescence response in the tissue for the treated and untreated skin samples. At the end of 24 hours, the dye penetrates the epidermis both in the case of passive diffusion as well as ultrasound as can be seen in **Fig. 2.26a,b**. However, there is a significant increase in dye permeation to the dermis in the case of ultrasound as can be visually appreciated in **Fig. 29b**. The percentage of tissue exhibiting fluorescence is plotted in **Fig. 29c**. Skin treated with ultrasound exhibits a 3.5-fold increase in dye concentration as compared to passive permeation. The results are significant with a p-value with 0.002.

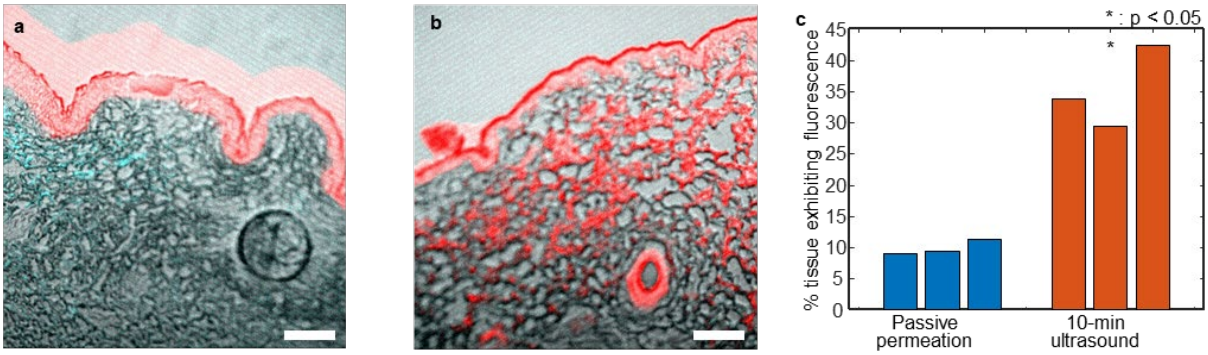

Figure 29 Multiphoton confocal microscopy images showing RhB penetration into a vertical section (7 µm thick) of a porcine skin sample for **a,** passive diffusion and **b,** 10-min ultrasound treatment. Scale bar, 200 µm. **c,** percentage of tissue exhibiting fluorescence across 6 samples of porcine skin (n = 3 passive diffusion, n = 3 10-min ultrasound). The confocal images are thresholded for fluorescence using ImageJ, details and raw images are given in **Appendix B6** and **Appendix A5**.

3. Conclusion and future work

Bulky and power consumptive equipment [71], long exposure times, and high variability between the permeability enhancement observed *in vivo* and *in vitro* have been cited as the main challenges to the successful deployment and adoption of transdermal drug delivery systems. Recently, wearable system concepts have been proposed that demonstrate good performance *in vivo* using HFS but few studies have characterized the working physics of the enhancement mechanisms required to guarantee repeatability. In this study, we use a combined theoretical and experimental approach to characterize and precisely control the ultrasound transducer deflection, device geometry, resulting pressure field and heat generation within the medium to induce cavitation in a repeatable manner using IFS. We characterize the threshold and strength of inertial cavitation using its acoustic subharmonic and broadband noise signature. We determine the threshold as the driving voltage for the cUSP elements which can be directly set and modulated by the user to linearly ramp the strength of cavitation. We use high-speed imaging to validate

the nucleation density and size of bubbles induced, and calculate the bubble streaming velocity close to the PZT-D surface. This acts as a quantitative indicator of the convective effect provided by the ultrasound system, where previously these effects are only qualitatively or theoretically discussed [22], [72], [73]. Finally, we demonstrate the efficacy of the IFS device *in vitro* by showing a 26.2-fold improvement in niacinamide transport and decreased skin resistance in a porcine Franz cell model. We present an innovative patch design that allows consistent positioning of the ultrasound transducer and provides a controlled-volume cavity for sustained cavitation activity. As discussed in **Table 1**, we demonstrate high enhancement ratios comparable to those obtained with large commercial, hand-held ultrasound probes with a remarkably compact and simplified ultrasound system.

To the best of our knowledge, this is the first conceptual demonstration of a wearable IFS system for effective and operator-independent transdermal delivery of cosmeceuticals outside of a clinical setting. Future iterations on the same could build on a number of aspects to further functionalize and tighten the system parameters for programmable drug delivery. The issue of heat generation within the patch can be addressed through various routes; (1) shortening the duty cycle or total ultrasound application time, and (2) adding heat-sinks in the form of a metallic or conductive polymeric mass on the backing of the PZT-Ds to dissipate the heat to the surrounding air. Further, dual-frequency ultrasound [74] in conjunction with heavy matching layers [52] can be applied alternatively to nucleate, grow and collapse the bubbles using the distinct effects achieved with each mode as seen in **Supplementary Video S5** and improve the abrasive and convective action of the bubbles. The formulation of the fluid couplant between the patch and the

skin can also be engineered in the form of a hydrogel to allow easy application by the user. The physicochemistry of this hydrogel can be carefully tailored to include more nucleation seeds (such as micro gas bubbles with a stabilizing phospholipid shell) for more vigorous onset of cavitation. However, as per the scope of this work, we focus on the improvements for the biomechanical integration and wearability of the patch as given below.

An immediate iteration possible on this design involves replacing the 2 mm-thick PZT-Ds with thinner discs (< 1 mm thickness). As the radial mode of operation of the disc has been selected, changing the thickness of the disc will cause a negligible shift on the radial resonance mode. This reduces the overall thickness while allowing better flush contact with the skin. The conformability and fit of the patch to curvilinear tissue such as the cheek can be characterized using FEM simulations for initial predictions on stretchability and radius of curvature along various axes, and can be experimentally evaluated using a pressure-sensitive tape between the patch and skin. The design and mechanical properties of the piezoelectric components and polymer encapsulation should be tailored for better biomechanical integration with the soft facial skin [75], [76].

In this system, the cUSP delivers treatment to the areas of the skin directly below the 2D array of the PZT-Ds (each 0.8 cm^2). This is an intermediate-zone in terms of spatial targeting as compared to highly localized treatments such as hypodermic needles or microjetting[77], [78] (10-100 micron jet/needle diameter) and uniform treatments over large areas of the skin such as with microneedle patches or Dermarollers[79]. This phenomenon of creation of localized transport regions (LTRs) has been observed and characterized in previous literature [74],[30]. For transdermal drugs destined to take action

within skin (epidermis and dermis layers), the cUSP achieves superior performance (13.2-fold larger) compared to 200 micron microneedles. While longer microneedles or pulsed microjets may enable higher drug penetration depths and volumes, there is a trade-off with pain, invasiveness and bruising that makes them less desirable than the cUSP. Further, needle-free microjet injections require sophisticated microfluidic devices and high-power pulsed laser setups [80], making them unsuitable for wearable applications. In this sense, the cUSP is a realization of a compact, wearable interface for effective and pain-free drug delivery to targeted zones of the skin. In future iterations, this unique capability of the cUSP can be leveraged with computer vision to extract texture and coloration information from a 3D scan of the users face and provide auto-placement and packing of the PZT-Ds to provide targeted treatment to spots or scars. Such customized embodiments of the cUSP can then be used to conduct in vivo studies to study disease progression in human subjects over a span of months.

To further miniaturize the cUSP interface, other transducer configurations and operation modes can be considered. For example, bending modes on unimorph or bimorph piezoelectric cantilevers allow creation of high acoustic pressures with smaller driving voltages. A radial array of such devices would also provide higher spatial efficiency (in the thickness direction) while covering the same surface area as bulk disc transducers.

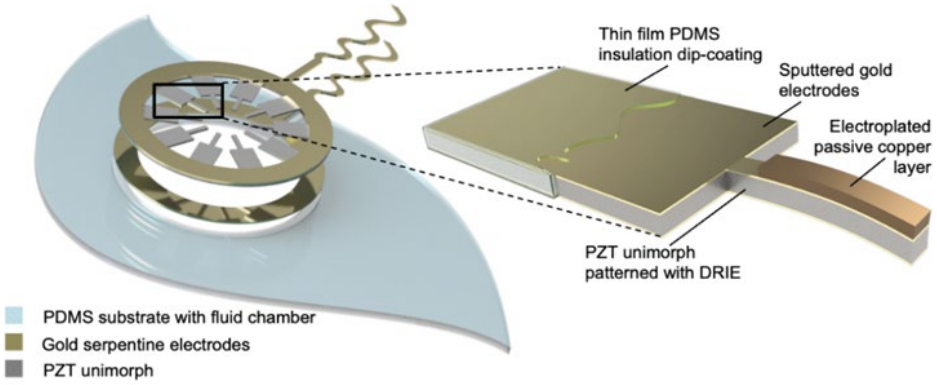

Figure 30 Conceptual illustration of a unimorph cantilever based sonophoresis interface

We conducted a preliminary study with our collaborators at the University of Buffalo to theoretically investigate the acoustic pressure generated with such devices. A 300 μm thick PZT bimorph cantilever (3 mm long, 1 mm wide) is considered in parallel circuiting configuration as shown in **Fig. 31b**. It is driven at its second resonant mode at 165 kHz. This mode is chosen as the resonance frequency is comparable to the radial mode frequency used with bulk PZT-D (220 kHz), ensuring commensurability between the cavitation thresholds in the two cases. We see that the cantilevered configuration is capable of generating a higher peak pressure (350 kPa as compared to 100 kPa with the PZT-D) at a smaller driving voltage (25 V as compared to 50 V).

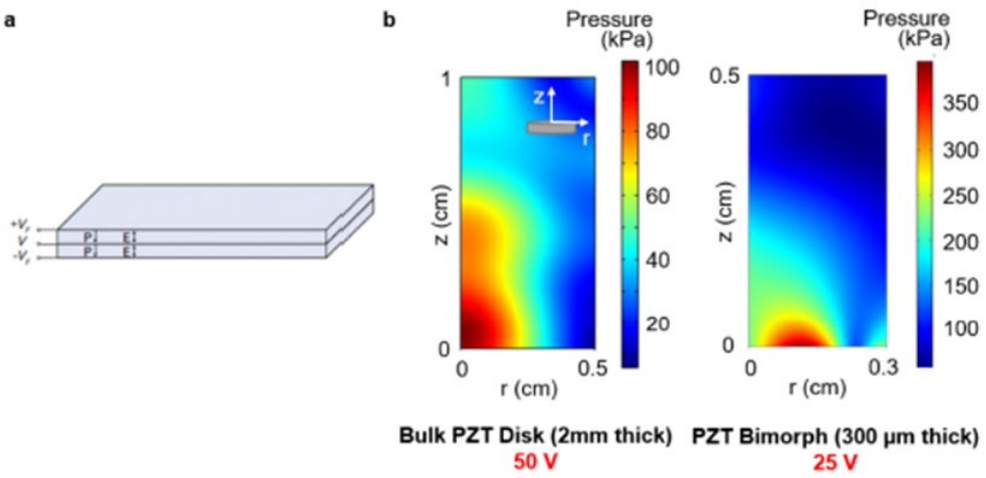

Figure 31 Comparison of peak acoustic pressure and acoustic pressure distribution with bimorph cantilevers as compared to bulk PZT-Ds. **a,** Parallel circuiting of a bimorph cantilever **b,** Acoustic pressure distribution and peak acoustic pressure obtained with bulk PZT-D (left) and bimorph actuator (right) at the listed driving voltages.

This demonstrates the feasibility of using bending mode transducers to effect further miniaturization and energy efficiency of the patch.

Finally, methods need to be devised for creating an adhesive interface between the device and the skin. In the current configuration of the patch, biocompatible Tegaderm tape could be used on the underside of the patch to adhere it to the skin. However, more robust and long-term approaches need to be explored to ensure repeatable use of the patch. Materials that are innately sticky such as polyimide or partially cured PDMS can be incorporated into the polymeric substrate. Alternatively, exposure to a brief UV treatment can be used to enhance the tackiness of the polymeric substrate before attachment to the face.

This work makes an important contribution through the rigor of the framework presented for end-to-end design and performance characterization of a rigid-flexible system of ‘wearable ultrasound’ devices. There is a need for a prescriptive framework for

performance characterization within which to streamline efforts for material discovery and device engineering of ultrasound-based drug delivery devices. In this study we present the complete gamut of bi-modal characterization methods (simulation and experiment), fabrication techniques and *in vitro* testing outcomes of a first-of-its-kind prototype of a wearable intermediate-frequency sonophoresis device. The learnings bear potential to greatly accelerate material exploration and optimized design of all components of the system; the rigid ultrasound transducer, polymeric substrate and fluid coupling medium. With further miniaturization of the transducer and the electronics module, we envision this device providing a game-changing alternative to oral and needle-based delivery of intramuscular small-molecule (<500 Da) drugs [81].

Appendix A

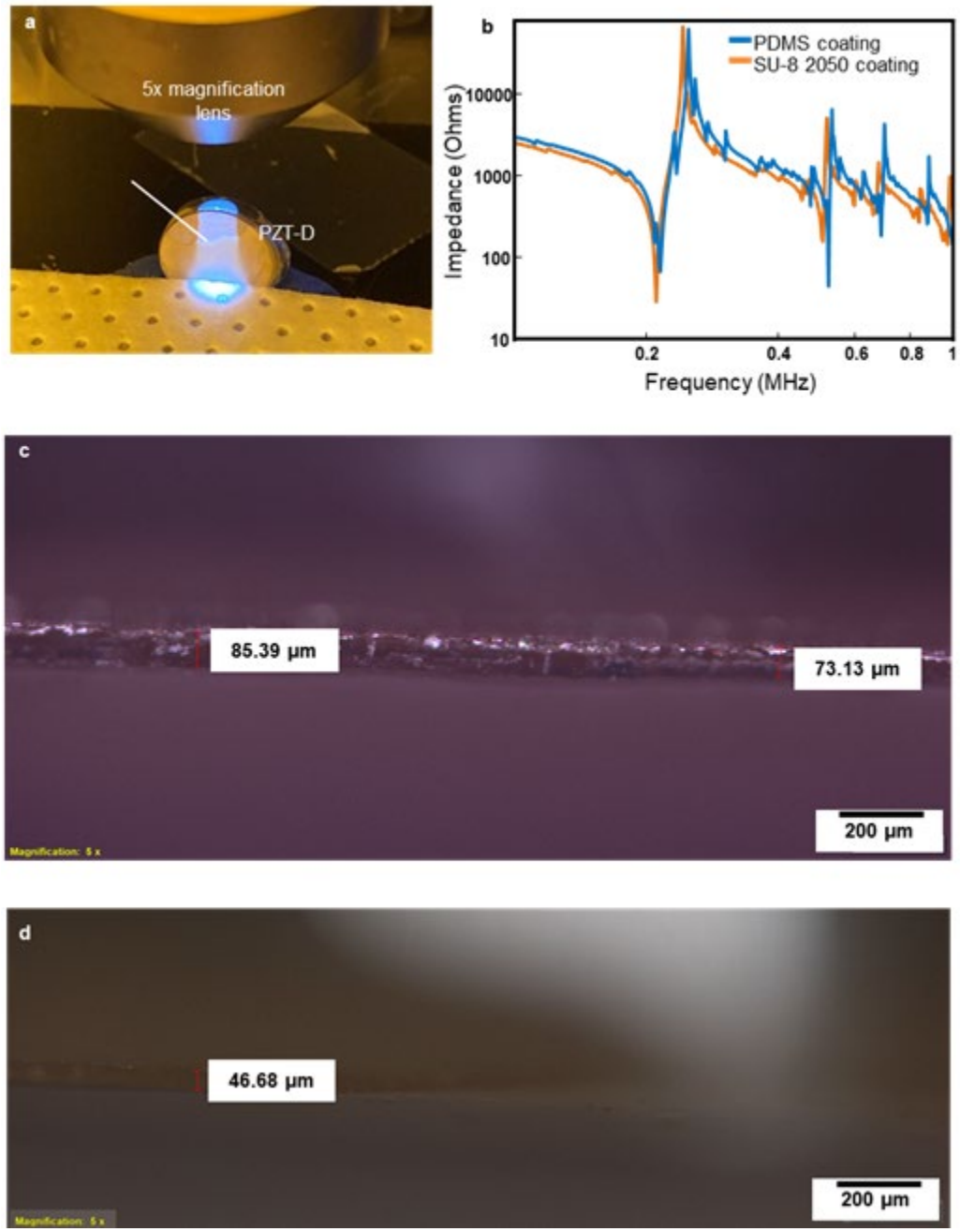

Appendix A1 | a, Coating thickness measurement setup. **b,** Impedance plots for single element PZT-Ds with two different coatings – PDMS and SU-8 2050. **c,** PDMS coating thickness (average thickness, ~80 µm) **d,** SU-8 2050 coating thickness (average thickness, 47.5 µm)

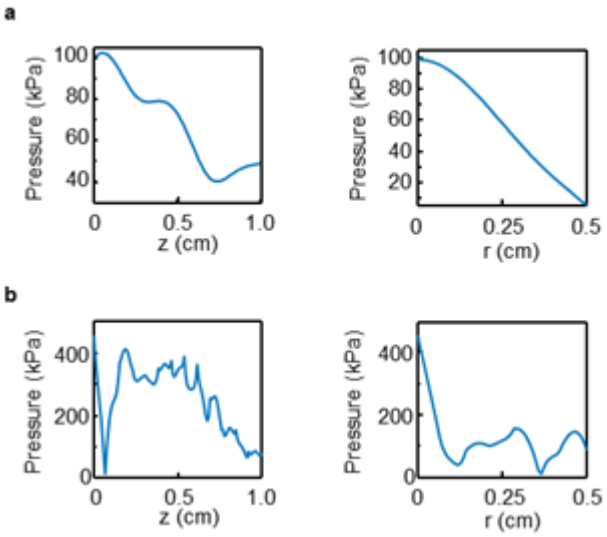

Appendix A2 | Drop-off of pressure with distance in the axial (z) and radial (r) directions at the 2 resonant modes at **a,** 212 kHz and **b,** 1 MHz.

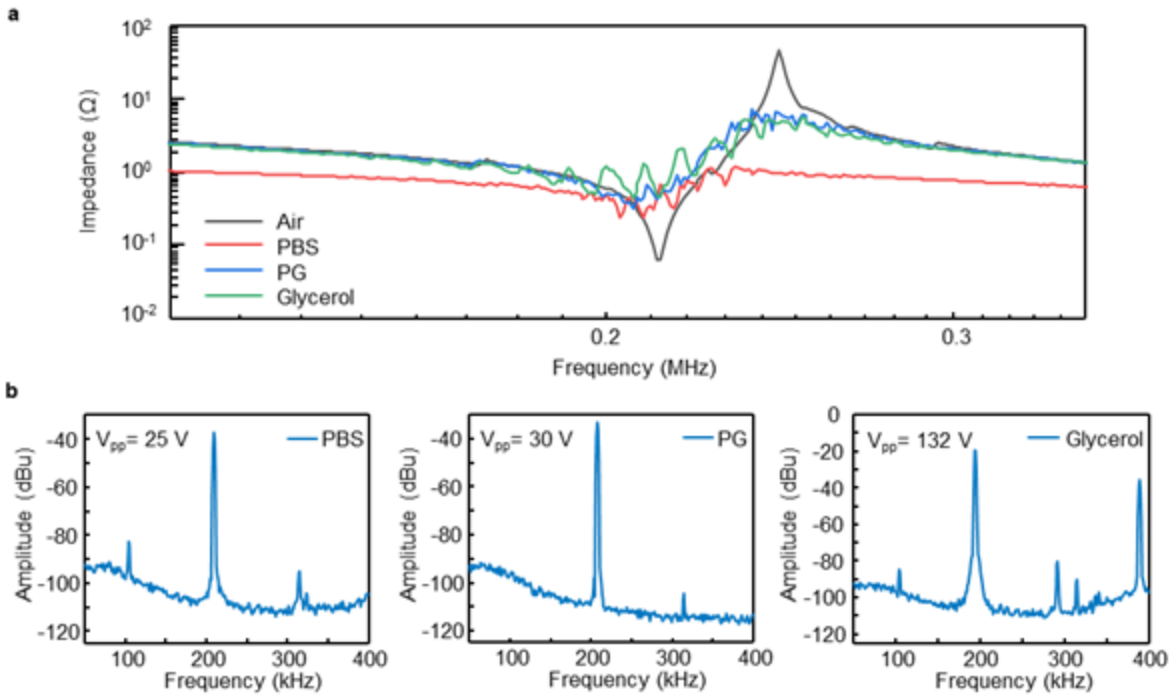

Appendix A3 | a, Impedance plot showing damping effect of various fluid mediums on PZT-D. The damping can be qualitatively assessed by **b,** Cavitation threshold voltage (measured by first appearance of ultra-subharmonic peak in acoustic spectrum) for different buffers (PBS, PG and glycerol).

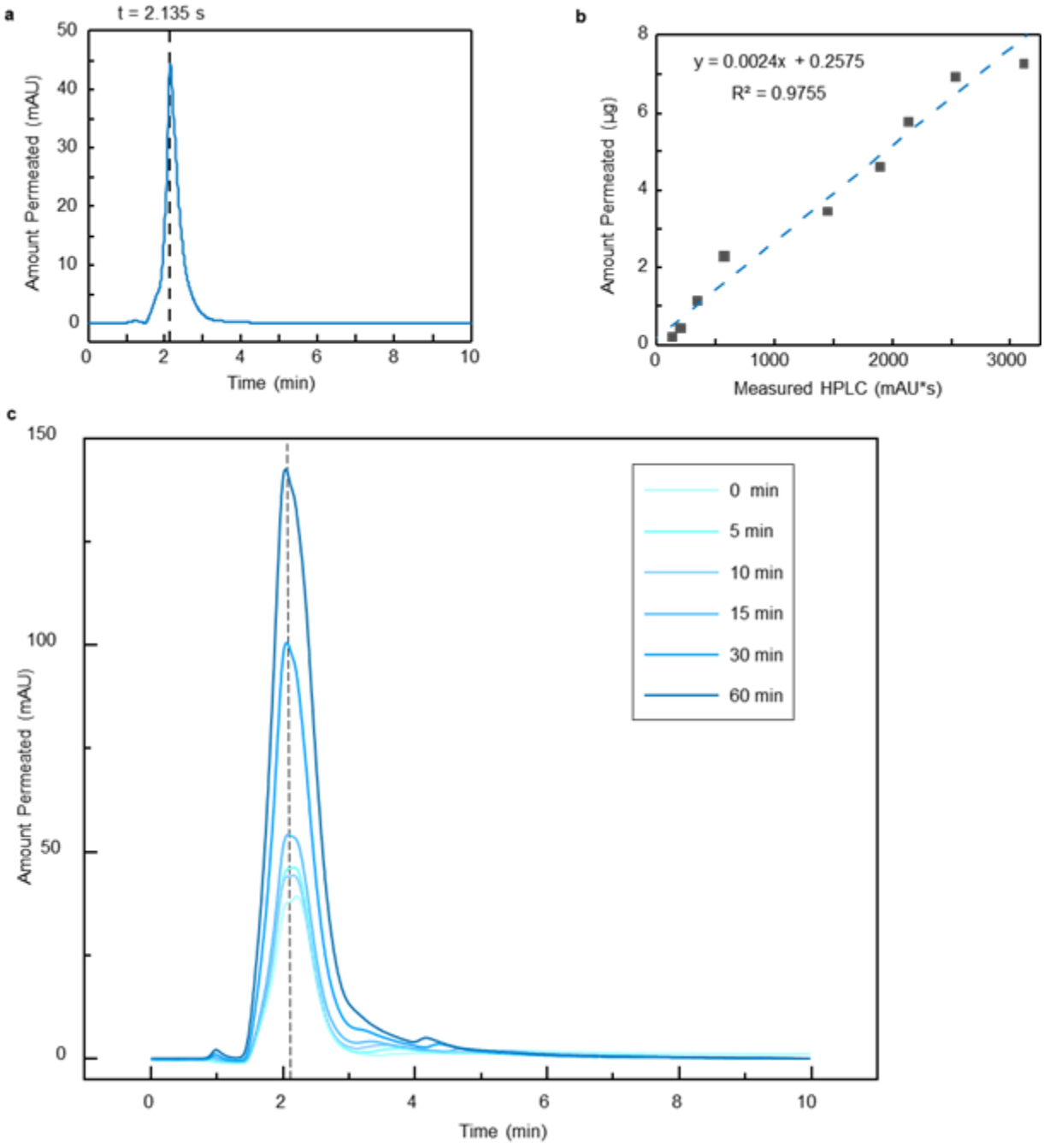

Appendix A4 | a, Representative HPLC measurement result for NIA solution. . The dotted line marks the time of elution of NIA (2.1 minutes). **b,** Dilution curve for the measured HPLC data. A best fit line was constructed and its equation was used to back-calculate the HPLC values from the arbitrary unit scale (mAU*s) to micrograms. **c,** Time series HPLC data from a sample solution (T7) extracted from the receptor chamber in a Franz cell treated with 10-minute ultrasound at 50 V_{pp}, 50% duty cycle, taken at different time points from t = 0 to t = 60 minutes. The dotted line marks the time of elution of NIA (2.1 minutes).

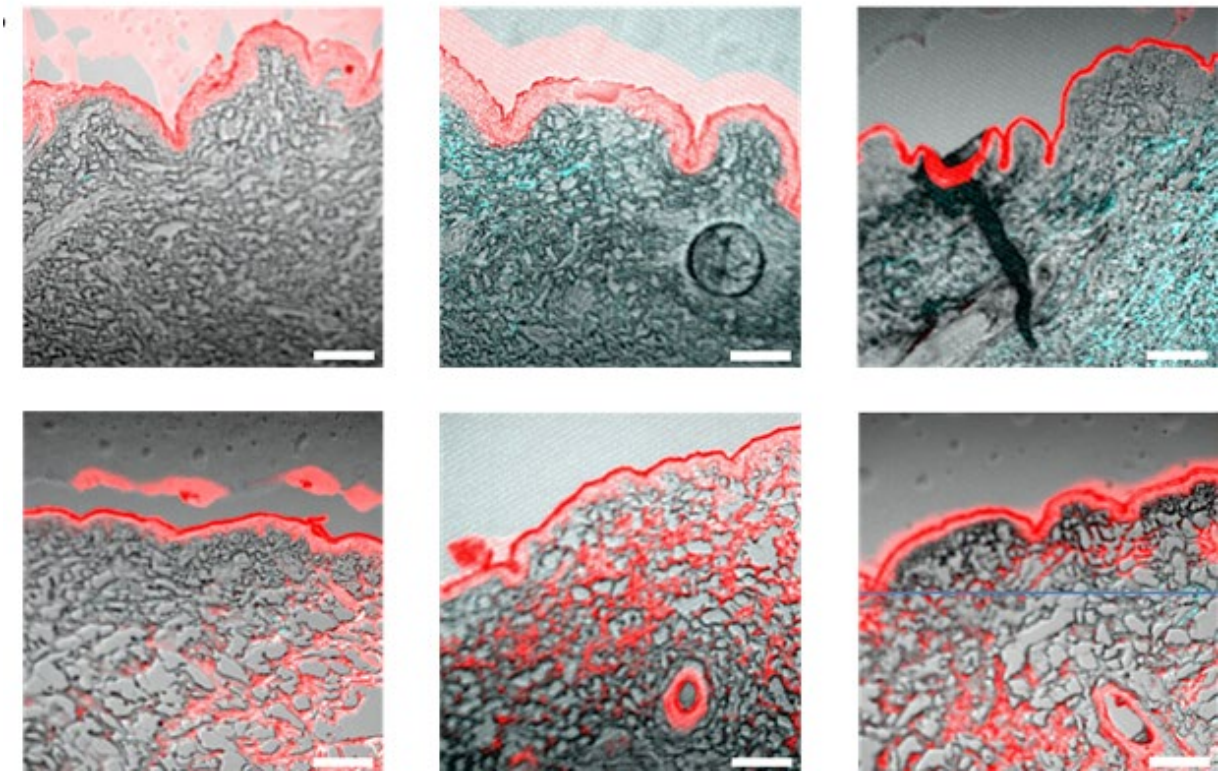

Appendix A5 | Multiphoton confocal microscopy images showing RhB penetration into a vertical sections (7 µm-thick) of 6 porcine skin samples for **(top row),** n = 3 samples for passive diffusion and (**bottom row),** n = 3 samples for 10-min ultrasound treatment. Scale bar, 200 µm.

Appendix B

Appendix B1

Piezoelectric transducer coating (Single-element). The surface of the piezoelectric disc (each weighing 1.2 g, Steiners and Martins, Inc.) was cleaned using isopropyl alcohol and DI water, and a small piece of copper tape (thickness = 75 μm) was used to make flexible connections to a shielded coax cable. The device was then encapsulated using a dip-coating method. First, the PZT-D was dipped in Omnicoat (Kayaku Advanced Materials, Inc.) and baked at 150 ℃ for 1 minute. It was then dipped into SU-8 2050 photoresist (Kayaku Advanced Materials, Inc.), followed by a ramped bake from 65-95 ℃ for 1.5 hours to promote photoresist reflow and prevent the build-up of thermal stress and wrinkles in the coating. A flood UV (405 nm) dose of 350 mJ was then applied to the coating on all four sides to cure the photoresist, followed by a hard bake at 95 ℃ for 15 minutes. Please note that this coating process is applicable to the single-element PZT-Ds used in the measurements for electromechanical, pressure and cavitation characterization of individual transducers. The PZT-Ds in the 2D array patch are coated directly in PDMS to facilitate better bonding of the coated PZT-D with the PDMS base substrate [82]. The impedance of the piezoelectric device was monitored in air before coating, and in air and water after coating to estimate the damping and ensure water-tightness.

Fabrication of 2D array patch. The bulk piezoelectric discs were dip-coated in polydimethylsiloxane (PDMS, Sylgard 184, Dow Corning) and cured at 100 ℃ for 1 hour. The electrodes were covered with a small piece of Kapton tape that was peeled-off after the dip-coating to expose the pads for connection to the circuit. For electrical connections to the device, standard photolithography was used to fabricate the copper interconnects on a 36 μm thick copper foil (EMI Copper Foil Shielding Tape 1181, 3M). Several drops of AZP4620 photoresist (Microchemicals GmbH) was dispensed onto the copper foil attached on a silicon wafer and the whole substrate was spun at 1500 rpm for 45 seconds using a spin coater (PWM50, Headway Research). The substrate was then baked at 95 ℃ for 2 minutes followed by 110 ℃ for 2 minutes on a hotplate (VWR International). To define the serpentine pattern, the substrate was exposed to UV at 403 nm under a transparency mask for 15 seconds, developed using the AZ400K developer (AZ Electronic Materials®) , and baked at 120 ℃ for 5 minutes. Next, the substrate was placed in a bath of copper etchant (Type CE-100, Transene Company Inc.) at 120 ℃ for 1 hour to remove the exposed copper. Lastly, to dissolve the underlying adhesive, the substrate was soaked in a bath of AZ400T stripper (AZ Electronic Materials®) at 120 ℃ until the serpentine pattern was lifted off. The electrode was then dried off and ready for subsequent assembly. To assemble the array, the coated PZT-D elements were positioned in a 3-D printed (FDM Prusa i3 MK3S+) poly-lactic acid filament mold with a 20 mm distance between adjacent elements. The serpentine electrode was then positioned in the mold and attached to the electrodes on the back side of the PZT-D elements with solder paste. Copper wires were then soldered to the top side of the copper foil for electrical connection. Part A and Part B of PDMS were mixed at 10:1 weight ratio

thoroughly, degassed in a vacuum chamber, and poured into the mold to a thickness of 4 mm to completely encapsulate the PZT-D elements and the serpentine interconnects.

Appendix B2

High-speed imaging. A coated PZT-D was suspended in a large water tank (dimensions 26.0 x 26.0 x 26.0 cm) lined with acoustic absorber panels. Phantom v2512 high-speed camera (Vision Research Inc.) was used with two 2x teleconverter lenses (Nikon, Tamron) to achieve up to a 4X magnification of the imaging zone close to the PZT-D surface. A 150 W halogen fiber optic illumination source (AmScope) was used to provide sufficient illumination for high-frame rate (10,000 fps), low exposure image capture. The light source was sealed in a plastic ziploc bag and submerged under the water to provide sufficient illumination close to the PZT-D. A millimeter scale was placed at the focal plane to calibrate the pixel size in the image for bubble size and velocity calculations. The footage was recorded using the custom PCC Software and exported to a .tif stack for post-processing and analysis on ImageJ. For bubble size characterization, the frames were visually inspected to select in-focus bubbles, and a circle and bounding box were used to measure the bubble diameter. A total of 60 bubbles were selected across 3 frames and a histogram of their radii is provided in Supplementary Fig. S11. For the bubble count analysis, a single stream of bubbles was manually selected across a substack of 250 frames. The total pixel area under analysis was kept constant at 12,000±500 pixels. Contrast enhancement was used where appropriate and the figure was then thresholded to select the bubbles and apply false color. A watershed technique was applied to separate any lumped bubble outlines. A particle analyzer was then used to count the total number of bubbles within a certain size/circularity range. This was then

divided by the total number of frames to give the average bubble count per frame. For the velocity measurements, a single bubble was tracked from its origin at the PZT-D surface until it reaches the first pressure node at a distance of around 1 cm where it oscillates more or less in place. A straight line is drawn and measured using the calibration scale between these points and the distance is divided by the number of frames and the duration of each frame (20 ms) to yield the velocity in m/s.

Appendix B3

Skin preparation and processing for *in vitro* permeation study. Porcine ear skin (Animal Technologies) (shaved, cut in pieces of approximately 3x4 mm, frozen at -20 ℃) was placed in a ziploc bag and thawed in water at room temperature for 15 minutes. The skin was then hydrated in phosphate-buffered saline (PBS, Corning) for 15 minutes. The thickness of the skin was measured with a caliper just before it was assembled in the Franz cell, and the edges of the skin outside the cell were trimmed to prevent evaporation during the experimental process.

Franz Cell setup for *in vitro* permeation study. A custom fixture was designed and 3D printed using poly-lactic acid (PLA) for the Franz Cell study. The top and bottom halves of the Franz Cell incorporate holders for 4 mm Ag/AgCl electrodes (BMD-4, BioMed Products Inc.) which are suspended 1 mm above the surface on either side of the skin once the cell is assembled. Once filled, a conductive PBS pathway is created across the skin and the resistance can be calculated using a voltage divider circuit. A function generator (400 3A, BK Precision) is used to apply a 10 Hz sinusoidal signal (100 mV peak-to-peak) to the skin and the following equation is used to estimate the resistivity.

$$R_{\text{skin}}(t) = \left(\frac{V_{\text{out}}}{V_{\text{r}}} - 1\right) R_{\text{k}} - R_{\text{fgen}} - R_{\text{PBS}},$$

, where V_{out} is the voltage at the input of the measurement circuit, and V_r is the voltage drop across a known resistor R_k.

The Franz cell was assembled with the porcine skin tightly clamped between the donor and receptor chambers and placed in a hot water bath maintained at 32 ℃. A magnetic stirrer was used to agitate the solution at 100 rpm. The bottom cell was filled with PBS as the receptor solution. The choice for the solvent in the donor solution was selected based on experiments to quantify the cavitation thresholds for different solvents (**Appendix A3**). The resonant frequency shift (as measured from the impedance curve) as well as the cavitation threshold were the lowest for PBS. Thus, a 3% w/w NIA/PBS was used as the donor solution. The single-element coated PZT-D was positioned at 1 mm from the skin surface using a fixture inside the Franz cell and a pulsed sinusoidal signal (f_r, 50 V_{pp}, 50% duty cycle, 5000 cycles ON/OFF) was applied. 200 µL samples were collected from the receptor at designated time intervals (t = 5 min, 10 min, 15 min, 30 min, and 1 hour) and replenished with an equal amount of PBS.

For the thermal control study, an infrared thermal camera (FLIR C2, Teledyne FLIR LLC) was used to monitor the temperature rise in the Franz cell due to heat generation by the ultrasound device. An in-depth study was conducted using a calibrated commercial thermocouple logger (EL-USB-TC-LCD, EasyLog) to measure the temperature profile of the solution in the donor chamber using a PBS solution and PDMS membrane to simulate the skin. The same temperature profile was then applied using a resistive heating element

(10 W, 5 ohm) and microcontroller (SAMD21E, Atmel) to mimic the thermal ramp observed with the ultrasound transducer.

To demonstrate the applicability and efficacy of the 2D array patch, a larger custom Franz cell fixture was designed and 3D printed using poly-lactic acid (**Fig. 2.21**). The experiment protocol was identical to the Franz cell permeation study using the single-element PZT-D. It is to be noted however that the power used to drive the 2D array patch (4 PZT-D elements) ranged from 3.6-4.8 W, while the power used to drive a single PZT-D element ranged from 1.05-1.3 W.

Appendix B4

Data Analysis for the in vitro permeation study. To quantify the amount of NIA permeation, high-performance liquid chromatography (HPLC) was performed on a 65 µl sample using a Series 1100 HPLC machine (Hewlett Packard). The samples were run in an 20:80 methanol:water isocratic column for 10 minutes, with the NIA peak emerging at 2.1 minutes as established by a pure NIA solution as a baseline (Supplementary Fig. S10a). The HPLC data is recorded in amount (unit: mAU) versus time (unit: s), and the height of the peak (unit: mAU) represents the amount of NIA present in the solution. To quantify the amount permeated in standard SI units, a standard curve was established by performing a serial dilution of NIA/PBS samples with known concentrations (**Appendix A4**). The amount of NIA permeated was then converted to units of µg/cm^2 using the standard curve. The result was scaled with the volume ratio of the receptor chamber to the extracted sample, the initial skin resistance (with the largest value normalized to 1),

and the actively treated skin area in each case. In the single element study, the PZT-D covers 25% of the skin directly exposed to the ultrasonic field, while only 12.3% of the total skin area is covered by the 4 PZT-D elements in the larger Franz cell (Supplementary Fig. S10b). Thus, the amount of NIA permeation with ultrasound treatment was calculated by subtracting that of control/thermal control and dividing by the skin area directly exposed to the ultrasonic field.

The data was analyzed using OriginLab software. Results are presented as the mean ± standard deviation (SD). The one-way analysis of variance (ANOVA) with Tukey's post hoc test was used to analyze data between groups (ultrasound vs. thermal control vs. passive control for PZT-D and ultrasound vs. passive control for array). The Brown-Forsythe test was used to confirm homogeneity of variance. Statistical significance was assumed when the p value was less than 0.05.

Appendix B5

Dye permeation study. 1.5 cm x 1.5 cm pieces of skin are prepared as per the protocol given above and fixed in a diffusion cell (**Fig. 2.25**). The bottom chamber is filled with PBS to keep the skin hydrated on both ends through the study. A standard solution (1 mg/ml) of Rhodamine B (RhB, 479 $gmol^{-1}$ Sigma Aldrich) is prepared in PBS (Corning). 750 µl of the dye solution is pipetted into the top chamber. N = 3 cells are maintained for passive diffusion as controls, and are allowed to stand on the hot-plate for 24 hours. N = 3 cells are treated with 10 minutes of ultrasound at 50 V_{pp}, with a 50% duty cycle. A PZT-D coated in PDMS is suspended 1 -mm from the skin surface and submerged into the dye solution in the top chamber. After 24 hours, the cells are disassembled and the skin

surface is cleaned with a cotton swab to remove excess dye from the surface. The skin samples are then flash-frozen in an embedding matrix (Tissue-Tek O.C.T. Compound, Sakura Finetek) at -80℃ in a dry ice bath. A cryotome is used to process 7 μm-thick slices of the skin which are fixed on glass slides and imaged under a multiphoton confocal microscope (Olympus FV1000) using an 840 nm laser. ImageJ software is used to characterize the fluorescence response in the images. A binary thresholding operation is performed on both the transmitted optical image and the fluorescence image to select the regions of interest for the tissue structure and the fluorescing tissue respectively. An intersection of these pixel sets (using an AND operation in the ROI Manager) gives the fluorescence response for each sample. This set is divided by the number of pixels in the tissue structure set to yield a normalized measurement of the percentage of fluorescing tissue for each sample. The images from 6 slides (n = 3 passive diffusion, n = 3 10-min ultrasound) are given in **Appendix A5**.

References:

[1] C. Dhand, M. P. Prabhakaran, R. W. Beuerman, R. Lakshminarayanan, N. Dwivedi, and S. Ramakrishna, “Role of size of drug delivery carriers for pulmonary and intravenous administration with emphasis on cancer therapeutics and lung-targeted drug delivery,” *RSC Adv.*, vol. 4, no. 62, pp. 32673–32689, Jul. 2014, doi: 10.1039/C4RA02861A.

[2] K. Zhang *et al.*, “A continuous tri-phase transition effect for HIFU-mediated intravenous drug delivery,” *Biomaterials*, vol. 35, no. 22, pp. 5875–5885, Jul. 2014, doi: 10.1016/j.biomaterials.2014.03.043.

[3] C. Luo, J. Sun, Y. Du, and Z. He, “Emerging integrated nanohybrid drug delivery systems to facilitate the intravenous-to-oral switch in cancer chemotherapy,” *J. Control. Release Off. J. Control. Release Soc.*, vol. 176, pp. 94–103, Feb. 2014, doi: 10.1016/j.jconrel.2013.12.030.

[4] R. Diab, C. Jaafar-Maalej, H. Fessi, and P. Maincent, “Engineered nanoparticulate drug delivery systems: the next frontier for oral administration?,” *AAPS J.*, vol. 14, no. 4, pp. 688–702, Dec. 2012, doi: 10.1208/s12248-012-9377-y.

[5] M. R. Prausnitz and R. Langer, “Transdermal drug delivery,” *Nat. Biotechnol.*, vol. 26, no. 11, pp. 1261–1268, Nov. 2008, doi: 10.1038/nbt.1504.

[6] M. R. Prausnitz, S. Mitragotri, and R. Langer, “Current status and future potential of transdermal drug delivery,” *Nat. Rev. Drug Discov.*, vol. 3, no. 2, pp. 115–124, Feb. 2004, doi: 10.1038/nrd1304.

[7] B. W. Barry, “Novel mechanisms and devices to enable successful transdermal drug delivery,” *Eur. J. Pharm. Sci. Off. J. Eur. Fed. Pharm. Sci.*, vol. 14, no. 2, pp. 101–114, Sep. 2001, doi: 10.1016/s0928-0987(01)00167-1.

[8] G. M. Shingade, “REVIEW ON: RECENT TREND ON TRANSDERMAL DRUG DELIVERY SYSTEM,” *J. Drug Deliv. Ther.*, vol. 2, no. 1, Art. no. 1, Jan. 2012, doi: 10.22270/jddt.v2i1.74.

[9] N. V. D., N. SHRESTHA, and J. Sharma, “Transdermal drug delivery system: An overview,” *Int. J. Res. Pharm. Sci.*, vol. 3, Apr. 2012.

[10] D. Chantasart and S. K. Li, “Structure Enhancement Relationship of Chemical Penetration Enhancers in Drug Transport across the Stratum Corneum,” *Pharmaceutics*, vol. 4, no. 1, pp. 71–92, Jan. 2012, doi: 10.3390/pharmaceutics4010071.

[11] Q. D. Pham, S. Björklund, J. Engblom, D. Topgaard, and E. Sparr, “Chemical penetration enhancers in stratum corneum - Relation between molecular effects and barrier function,” *J. Control. Release Off. J. Control. Release Soc.*, vol. 232, pp. 175–187, Jun. 2016, doi: 10.1016/j.jconrel.2016.04.030.

[12] A. Z. Alkilani, M. T. C. McCrudden, and R. F. Donnelly, “Transdermal Drug Delivery: Innovative Pharmaceutical Developments Based on Disruption of the Barrier Properties of the stratum corneum,” *Pharmaceutics*, vol. 7, no. 4, pp. 438–470, Oct. 2015, doi: 10.3390/pharmaceutics7040438.

[13] C. M. Schoelhammer, “Use of Physical Enhancers for Gastrointestinal and Transdermal Drug Delivery,” Doctoral thesis, Massachussetts Institute of Technology, Cambridge, MA, USA, 2015. Accessed: Mar. 10, 2020. [Online]. Available: https://dspace.mit.edu/handle/1721.1/98714

[14] S. Dharadhar, A. Majumdar, S. Dhoble, and V. Patravale, “Microneedles for transdermal drug delivery: a systematic review,” *Drug Dev. Ind. Pharm.*, vol. 45, no. 2, pp. 188–201, Feb. 2019, doi: 10.1080/03639045.2018.1539497.

[15] J. W. Lee, J.-H. Park, and M. R. Prausnitz, “Dissolving microneedles for transdermal drug delivery,” *Biomaterials*, vol. 29, no. 13, pp. 2113–2124, May 2008, doi: 10.1016/j.biomaterials.2007.12.048.

[16] M. A. Luzuriaga, D. R. Berry, J. C. Reagan, R. A. Smaldone, and J. J. Gassensmith, “Biodegradable 3D printed polymer microneedles for transdermal drug delivery,” *Lab. Chip*, vol. 18, no. 8, pp. 1223–1230, 2018, doi: 10.1039/C8LC00098K.
[17] Y. N. Kalia, A. Naik, J. Garrison, and R. H. Guy, “Iontophoretic drug delivery,” *Adv. Drug Deliv. Rev.*, vol. 56, no. 5, pp. 619–658, Mar. 2004, doi: 10.1016/j.addr.2003.10.026.
[18] A.-R. Denet, R. Vanbever, and V. Préat, “Skin electroporation for transdermal and topical delivery,” *Adv. Drug Deliv. Rev.*, vol. 56, no. 5, pp. 659–674, Mar. 2004, doi: 10.1016/j.addr.2003.10.027.
[19] S. Paliwal, G. K. Menon, and S. Mitragotri, “Low-Frequency Sonophoresis: Ultrastructural Basis for Stratum Corneum Permeability Assessed Using Quantum Dots,” *J. Invest. Dermatol.*, vol. 126, no. 5, pp. 1095–1101, May 2006, doi: 10.1038/sj.jid.5700248.
[20] R. Rao and S. Nanda, “Sonophoresis: recent advancements and future trends,” *J. Pharm. Pharmacol.*, vol. 61, no. 6, pp. 689–705, Jan. 2010, doi: 10.1211/jpp.61.06.0001.
[21] A. Tezel and S. Mitragotri, “Interactions of Inertial Cavitation Bubbles with Stratum Corneum Lipid Bilayers during Low-Frequency Sonophoresis,” *Biophys. J.*, vol. 85, no. 6, pp. 3502–3512, Dec. 2003, doi: 10.1016/S0006-3495(03)74770-5.
[22] B. E. Polat, D. Blankschtein, and R. Langer, “Low-frequency sonophoresis: application to the transdermal delivery of macromolecules and hydrophilic drugs,” *Expert Opin. Drug Deliv.*, vol. 7, no. 12, pp. 1415–1432, Dec. 2010, doi: 10.1517/17425247.2010.538679.
[23] J. Park, H. Lee, G.-S. Lim, N. Kim, D. Kim, and Y.-C. Kim, “Enhanced Transdermal Drug Delivery by Sonophoresis and Simultaneous Application of Sonophoresis and Iontophoresis,” *AAPS PharmSciTech*, vol. 20, no. 3, p. 96, Jan. 2019, doi: 10.1208/s12249-019-1309-z.
[24] E. C. Jung *et al.*, “Effect of ultrasound and heat on percutaneous absorption of l-ascorbic acid: human in vitro studies on Franz cell and Petri dish systems,” *Int. J. Cosmet. Sci.*, vol. 38, no. 6, pp. 646–650, 2016, doi: https://doi.org/10.1111/ics.12350.
[25] SonoTarg, “SonoTarg.” https://sonotarg.com/cancer-therapy-technology/ (accessed Jul. 08, 2022).
[26] OxSonics Therapeutics, “OxSonics.” https://oxsonics.com/ (accessed Jul. 08, 2022).
[27] “Biomechanics for Pathology and Treatment,” in *Integrated Nano-Biomechanics*, Elsevier, 2018, pp. 101–146. doi: 10.1016/B978-0-323-38944-0.00004-8.
[28] D. Park, J. Won, G. Lee, Y. Lee, C. Kim, and J. Seo, “Sonophoresis with ultrasound-responsive liquid-core nuclei for transdermal drug delivery,” *Skin Res. Technol.*, vol. 28, no. 2, pp. 291–298, Mar. 2022, doi: 10.1111/srt.13129.
[29] K. Yasui, “Acoustic Cavitation,” in *Acoustic Cavitation and Bubble Dynamics*, in SpringerBriefs in Molecular Science. Cham: Springer International Publishing, 2018, pp. 1–35. doi: 10.1007/978-3-319-68237-2_1.
[30] B. E. Polat, D. Hart, R. Langer, and D. Blankschtein, “Ultrasound-mediated transdermal drug delivery: Mechanisms, scope, and emerging trends,” *J. Controlled Release*, vol. 152, no. 3, pp. 330–348, Jun. 2011, doi: 10.1016/j.jconrel.2011.01.006.
[31] T. Hakozaki, H. Takiwaki, K. Miyamoto, Y. Sato, and S. Arase, “Ultrasound enhanced skin-lightening effect of vitamin C and niacinamide,” *Skin Res. Technol. Off. J. Int. Soc. Bioeng. Skin ISBS Int. Soc. Digit. Imaging Skin ISDIS Int. Soc. Skin Imaging ISSI*, vol. 12, no. 2, pp. 105–113, May 2006, doi: 10.1111/j.0909-752X.2006.00186.x.
[32] V. P. Shah and H. I. Maibach, Eds., *Topical Drug Bioavailability, Bioequivalence, and Penetration*. Boston, MA: Springer US, 1993. doi: 10.1007/978-1-4899-1262-6.
[33] Z. Fan, D. Chen, and C. X. Deng, “Characterization of the Dynamic Activities of a Population of Microbubbles Driven by Pulsed Ultrasound Exposure in Sonoporation,”

Ultrasound Med. Biol., vol. 40, no. 6, pp. 1260–1272, Jun. 2014, doi: 10.1016/j.ultrasmedbio.2013.12.002.
[34] S. Mitragotri, D. Blankschtein, and R. Langer, “Ultrasound-Mediated Transdermal Protein Delivery,” *Science*, vol. 269, no. 5225, pp. 850–853, Aug. 1995, doi: 10.1126/science.7638603.
[35] S. Mitragotri, D. Blankschtein, and R. Langer, “Transdermal drug delivery using low-frequency sonophoresis,” *Pharm. Res.*, vol. 13, no. 3, pp. 411–420, 1996, doi: 10.1023/A:1016096626810.
[36] J. Liu, T. N. Lewis, and M. R. Prausnitz, “Non-Invasive Assessment and Control of Ultrasound-Mediated Membrane Permeabilization,” *Pharm. Res.*, vol. 15, no. 6, pp. 918–924, Jun. 1998, doi: 10.1023/A:1011984817567.
[37] T. Thanh Nguyen, Y. Asakura, S. Koda, and K. Yasuda, “Dependence of cavitation, chemical effect, and mechanical effect thresholds on ultrasonic frequency,” *Ultrason. Sonochem.*, vol. 39, pp. 301–306, Nov. 2017, doi: 10.1016/j.ultsonch.2017.04.037.
[38] J. E. Barger, “Thresholds of Acoustic Cavitation in Water,” *J. Acoust. Soc. Am.*, vol. 36, no. 5, pp. 1008–1009, May 1964, doi: 10.1121/1.2143151.
[39] H. Tang, C. C. J. Wang, D. Blankschtein, and R. Langer, “An investigation of the role of cavitation in low-frequency ultrasound-mediated transdermal drug transport,” *Pharm. Res.*, vol. 19, no. 8, pp. 1160–1169, 2002, doi: 10.1023/A:1019898109793.
[40] S. Mitragotri, “Effect of therapeutic ultrasound on partition and diffusion coefficients in human stratum corneum,” *J. Controlled Release*, vol. 71, no. 1, pp. 23–29, Mar. 2001, doi: 10.1016/S0168-3659(00)00344-8.
[41] S. Mitragotri and J. Kost, “Transdermal delivery of heparin and low-molecular weight heparin using low-frequency ultrasound,” *Pharm. Res.*, vol. 18, no. 8, pp. 1151–1156, 2001, doi: 10.1023/A:1010979010907.
[42] A. Boucaud *et al.*, “In vitro study of low-frequency ultrasound-enhanced transdermal transport of fentanyl and caffeine across human and hairless rat skin,” *Int. J. Pharm.*, vol. 228, no. 1–2, pp. 69–77, Oct. 2001, doi: 10.1016/S0378-5173(01)00820-1.
[43] J. Manikkath, A. R. Hegde, G. Kalthur, H. S. Parekh, and S. Mutalik, “Influence of peptide dendrimers and sonophoresis on the transdermal delivery of ketoprofen,” *Int. J. Pharm.*, vol. 521, no. 1–2, pp. 110–119, Apr. 2017, doi: 10.1016/j.ijpharm.2017.02.002.
[44] D. Durmus, G. Alayli, A. S. Goktepe, M. A. Taskaynatan, A. Bilgici, and O. Kuru, “Is phonophoresis effective in the treatment of chronic low back pain? A single-blind randomized controlled trial,” *Rheumatol. Int.*, vol. 33, no. 7, pp. 1737–1744, Jul. 2013, doi: 10.1007/s00296-012-2634-7.
[45] S. Mitragotri and J. Kost, “Low-Frequency Sonophoresis: A Noninvasive Method of Drug Delivery and Diagnostics,” *Biotechnol. Prog.*, vol. 16, no. 3, pp. 488–492, Jun. 2000, doi: 10.1021/bp000024+.
[46] A. Boucaud, M. A. Garrigue, L. Machet, L. Vaillant, and F. Patat, “Effect of sonication parameters on transdermal delivery of insulin to hairless rats,” *J. Controlled Release*, vol. 81, no. 1–2, pp. 113–119, May 2002, doi: 10.1016/S0168-3659(02)00054-8.
[47] S. Li *et al.*, “Stretchable Electronic Facial Masks for Sonophoresis,” *ACS Nano*, vol. 16, no. 4, pp. 5961–5974, Apr. 2022, doi: 10.1021/acsnano.1c11181.
[48] C. Yu *et al.*, “A Conformable Ultrasound Patch for Cavitation-Enhanced Transdermal Cosmeceutical Delivery,” *Adv. Mater.*, p. 2300066, Apr. 2023, doi: 10.1002/adma.202300066.
[49] J. Robertson and S. Becker, “Influence of Acoustic Reflection on the Inertial Cavitation Dose in a Franz Diffusion Cell,” *Ultrasound Med. Biol.*, vol. 44, no. 5, pp. 1100–1109, May 2018, doi: 10.1016/j.ultrasmedbio.2018.01.021.
[50] F. Iliopoulos, B. C. Sil, A. S. M. Monjur Al Hossain, D. J. Moore, R. A. Lucas, and

M. E. Lane, “Topical delivery of niacinamide: Influence of neat solvents,” *Int. J. Pharm.*, vol. 579, p. 119137, Apr. 2020, doi: 10.1016/j.ijpharm.2020.119137.
[51] J. Rooze, E. V. Rebrov, J. C. Schouten, and J. T. F. Keurentjes, “Dissolved gas and ultrasonic cavitation – A review,” *Ultrason. Sonochem.*, vol. 20, no. 1, pp. 1–11, Jan. 2013, doi: 10.1016/j.ultsonch.2012.04.013.
[52] C. Wang, C. Wang, N. Liu, Y. Lan, and W. Cao, “Optimize multilayer matching layer design for tone-burst underwater acoustic transducers,” *J. Acoust. Soc. Am.*, vol. 152, no. 3, pp. 1942–1950, Sep. 2022, doi: 10.1121/10.0014286.
[53] T. Terahara, S. Mitragotri, J. Kost, and R. Langer, “Dependence of low-frequency sonophoresis on ultrasound parameters; distance of the horn and intensity,” *Int. J. Pharm.*, vol. 235, no. 1–2, pp. 35–42, Mar. 2002, doi: 10.1016/s0378-5173(01)00981-4.
[54] W. J. Galloway, “An Experimental Study of Acoustically Induced Cavitation in Liquids,” *J. Acoust. Soc. Am.*, vol. 26, no. 5, pp. 849–857, Sep. 1954, doi: 10.1121/1.1907428.
[55] F. Caupin and E. Herbert, “Cavitation in water: a review,” *Comptes Rendus Phys.*, vol. 7, no. 9–10, pp. 1000–1017, Nov. 2006, doi: 10.1016/j.crhy.2006.10.015.
[56] C. Piao and J. O. Kim, “Vibration characteristics of a piezoelectric disk laminated with an elastic disk,” *J. Mech. Sci. Technol.*, vol. 30, no. 12, pp. 5351–5362, Dec. 2016, doi: 10.1007/s12206-016-1102-9.
[57] A. Hajati *et al.*, “Three-dimensional micro electromechanical system piezoelectric ultrasound transducer,” *Appl. Phys. Lett.*, vol. 101, no. 25, p. 253101, Dec. 2012, doi: 10.1063/1.4772469.
[58] K. Johnston, “The cavitation subharmonic signal: mechanistic source and optimised detection,” p. 198.
[59] N. Segebarth, O. Eulaerts, J. Reisse, L. A. Crum, and T. J. Matula, “Correlation between Acoustic Cavitation Noise, Bubble Population, and Sonochemistry,” *J. Phys. Chem. B*, vol. 106, no. 35, pp. 9181–9190, Sep. 2002, doi: 10.1021/jp0146566.
[60] H. Alavi Tamaddoni, A. P. Duryea, E. Vlaisavljevich, Z. Xu, and T. L. Hall, “Acoustic Methods for Increasing the Cavitation Initiation Pressure Threshold,” *IEEE Trans. Ultrason. Ferroelectr. Freq. Control*, vol. 65, no. 11, pp. 2012–2019, Nov. 2018, doi: 10.1109/TUFFC.2018.2867793.
[61] M. Ashokkumar, “The characterization of acoustic cavitation bubbles – An overview,” *Ultrason. Sonochem.*, vol. 18, no. 4, pp. 864–872, Jul. 2011, doi: 10.1016/j.ultsonch.2010.11.016.
[62] W. Gaertner, “Frequency Dependence of Ultrasonic Cavitation,” *J. Acoust. Soc. Am.*, vol. 26, no. 6, pp. 977–980, Nov. 1954, doi: 10.1121/1.1907464.
[63] L. Machet and A. Boucaud, “Transdermal Transport by Sonophoresis,” in *Percutaneous Absorption*, 5th ed.Boca Raton: CRC Press, 2021, pp. 619–638. doi: 10.1201/9780429202971-43.
[64] N. Yamashita, K. Tachibana, K. Ogawa, N. Tsujita, and A. Tomita, “Scanning electron microscopic evaluation of the skin surface after ultrasound exposure,” *Anat. Rec.*, vol. 247, no. 4, pp. 455–461, Apr. 1997, doi: 10.1002/(SICI)1097-0185(199704)247:4<455::AID-AR3>3.0.CO;2-Q.
[65] Y. J. Jung, J.-H. Yoon, N. G. Kang, S. G. Park, and S. H. Jeong, “Diffusion properties of different compounds across various synthetic membranes using Franz-type diffusion cells,” *J. Pharm. Investig.*, vol. 42, no. 5, pp. 271–277, Oct. 2012, doi: 10.1007/s40005-012-0040-5.
[66] Y. Zhang, C.-P. Kung, F. Iliopoulos, B. C. Sil, J. Hadgraft, and M. E. Lane, “Dermal Delivery of Niacinamide—In Vivo Studies,” *Pharmaceutics*, vol. 13, no. 5, p. 726, May 2021, doi: 10.3390/pharmaceutics13050726.
[67] G. Merino, Y. N. Kalia, M. B. Delgado-Charro, R. O. Potts, and R. H. Guy,

"Frequency and thermal effects on the enhancement of transdermal transport by sonophoresis," *J. Controlled Release*, vol. 88, no. 1, pp. 85–94, Feb. 2003, doi: 10.1016/S0168-3659(02)00464-9.
[68] S. Mitragotri, J. Farrell, H. Tang, T. Terahara, J. Kost, and R. Langer, "Determination of threshold energy dose for ultrasound-induced transdermal drug transport," *J. Controlled Release*, vol. 63, no. 1, pp. 41–52, Jan. 2000, doi: 10.1016/S0168-3659(99)00178-9.
[69] K. T. Rich, C. L. Hoerig, M. B. Rao, and T. D. Mast, "Relations between acoustic cavitation and skin resistance during intermediate- and high-frequency sonophoresis," *J. Controlled Release*, vol. 194, pp. 266–277, Nov. 2014, doi: 10.1016/j.jconrel.2014.08.007.
[70] Y. Zhang *et al.*, "A comparison of the in vitro permeation of niacinamide in mammalian skin and in the Parallel Artificial Membrane Permeation Assay (PAMPA) model," *Int. J. Pharm.*, vol. 556, pp. 142–149, Feb. 2019, doi: 10.1016/j.ijpharm.2018.11.065.
[71] M. A. Oberli, C. M. Schoellhammer, R. Langer, and D. Blankschtein, "Ultrasound-enhanced transdermal delivery: recent advances and future challenges," *Ther. Deliv.*, vol. 5, no. 7, pp. 843–857, Jul. 2014, doi: 10.4155/tde.14.32.
[72] K. Tachibana and S. Tachibana, "Use of Ultrasound to Enhance the Local Anesthetic Effect of Topically Applied Aqueous Lidocaine," *Anesthesiology*, vol. 78, no. 6, pp. 1091–1096, Jun. 1993, doi: 10.1097/00000542-199306000-00011.
[73] H. Tang, S. Mitragotri, D. Blankschtein, and R. Langer, "Theoretical Description of Transdermal Transport of Hydrophilic Permeants: Application to Low-Frequency Sonophoresis," *J. Pharm. Sci.*, vol. 90, no. 5, pp. 545–568, May 2001, doi: 10.1002/1520-6017(200105)90:5<545::AID-JPS1012>3.0.CO;2-H.
[74] C. M. Schoellhammer *et al.*, "Applicability and safety of dual-frequency ultrasonic treatment for the transdermal delivery of drugs," *J. Controlled Release*, vol. 202, pp. 93–100, Mar. 2015, doi: 10.1016/j.jconrel.2015.02.002.
[75] C. Dagdeviren *et al.*, "Conformal piezoelectric systems for clinical and experimental characterization of soft tissue biomechanics," *Nat. Mater.*, vol. 14, no. 7, pp. 728–736, Jul. 2015, doi: 10.1038/nmat4289.
[76] Y. Su, S. Li, R. Li, and C. Dagdeviren, "Splitting of neutral mechanical plane of conformal, multilayer piezoelectric mechanical energy harvester," *Appl. Phys. Lett.*, vol. 107, no. 4, p. 041905, Jul. 2015, doi: 10.1063/1.4927677.
[77] K. Cu, R. Bansal, S. Mitragotri, and D. Fernandez Rivas, "Delivery Strategies for Skin: Comparison of Nanoliter Jets, Needles and Topical Solutions," *Ann. Biomed. Eng.*, vol. 48, no. 7, pp. 2028–2039, Jul. 2020, doi: 10.1007/s10439-019-02383-1.
[78] J. Krizek, P. Delrot, and C. Moser, "Repetitive regime of highly focused liquid microjets for needle-free injection," *Sci. Rep.*, vol. 10, no. 1, p. 5067, Mar. 2020, doi: 10.1038/s41598-020-61924-0.
[79] A. Singh and S. Yadav, "Microneedling: Advances and widening horizons," *Indian Dermatol. Online J.*, vol. 7, no. 4, p. 244, 2016, doi: 10.4103/2229-5178.185468.
[80] A. Arora *et al.*, "Needle-free delivery of macromolecules across the skin by nanoliter-volume pulsed microjets," *Proc. Natl. Acad. Sci.*, vol. 104, no. 11, pp. 4255–4260, Mar. 2007, doi: 10.1073/pnas.0700182104.
[81] B. C.-Q. Seah and B. M. Teo, "Recent advances in ultrasound-based transdermal drug delivery," *Int. J. Nanomedicine*, vol. 13, pp. 7749–7763, Nov. 2018, doi: 10.2147/IJN.S174759.
[82] M. A. Eddings, M. A. Johnson, and B. K. Gale, "Determining the optimal PDMS–PDMS bonding technique for microfluidic devices," *J. Micromechanics Microengineering*, vol. 18, no. 6, p. 067001, Jun. 2008, doi: 10.1088/0960-1317/18/6/067001.